

See discussions, stats, and author profiles for this publication at: <https://www.researchgate.net/publication/328053514>

# Architected Cellular Piezoelectric Metamaterials: Thermo-Electro-Mechanical Properties

Article in *Acta Materialia* · October 2018

DOI: 10.1016/j.actamat.2018.10.001

---

CITATIONS

30

READS

1,120

2 authors, including:

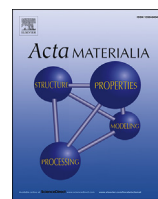


Jiahao Shi

McGill University

23 PUBLICATIONS 326 CITATIONS

SEE PROFILE



## Full length article

# Architected cellular piezoelectric metamaterials: Thermo-electro-mechanical properties

J. Shi <sup>a</sup>, A.H. Akbarzadeh <sup>a, b,\*</sup><sup>a</sup> Department of Bioresource Engineering, McGill University, Island of Montreal, QC, H9X 3V9, Canada<sup>b</sup> Department of Mechanical Engineering, McGill University, Montreal, QC, H3A 0C3, Canada

## ARTICLE INFO

## Article history:

Received 20 June 2018

Received in revised form

3 September 2018

Accepted 1 October 2018

Available online 3 October 2018

## Keywords:

Cellular piezoelectric metamaterial

Asymptotic homogenization

Piezoelectricity

Pyroelectricity

Multifunctional materials

## ABSTRACT

Advances in additive manufacturing have recently made possible the manufacturing of smart materials with arbitrary microarchitectures, which leads to developing lightweight smart metamaterials with unprecedented multifunctional properties. In this paper, asymptotic homogenization (AH) method is developed for predicting the effective thermo-electro-mechanical properties of architected cellular piezoelectric metamaterials. The effect of pore microarchitecture (relative density and cell topology) and polarization direction on elastic, dielectric, piezoelectric, pyroelectric and thermal properties of periodic cellular piezoelectric metamaterials is explored. The pore topology is determined by Fourier series expansion. Alternative pore microarchitectures are considered by tailoring shape parameters, scaling factor, and rotation angle of the constitutive pore. Smart cellular metamaterials made of both single-phase ( $\text{BaTiO}_3$ ) and bi-phase ( $\text{BaTiO}_3$ -epoxy) piezoelectric materials are considered. Apart from effective thermo-electro-mechanical properties, a series of figures of merit for the cellular piezoelectric metamaterials, i.e. piezoelectric coupling constant, acoustic impedance, piezoelectric charge coefficient, hydrostatic figure of merit, current responsivity, voltage responsivity and pyroelectric energy harvesting figures of merit, are presented and the reason for difference between the figures of merit of different types of piezoelectric metamaterials is discussed. The figures of merit shed lights on the effect of microarchitecture on optimizing the multifunctional performance of smart cellular metamaterials for applications as structurally efficient multifunctional energy harvesters. It is found that the piezoelectric and pyroelectric figures of merit of cellular piezoelectric metamaterials can be significantly improved compared to the commonly used honeycomb cellular materials and composite materials with solid circular inclusion if an appropriate microarchitecture is selected for the pore. For example, piezoelectric charge coefficient ( $d_h$ ) for a transversely polarized single-phase cellular piezoelectric metamaterial with a solid volume fraction of 0.4 can be 350% higher than the corresponding figures of merit of honeycomb piezoelectric material; voltage responsivity of transversely polarized bi-phase cellular piezoelectric metamaterials with an inclusion volume fraction of 0.3 can be also 249% higher than the corresponding value of composite materials with a solid circular inclusion.

© 2018 Acta Materialia Inc. Published by Elsevier Ltd. All rights reserved.

## 1. Introduction

By tailoring their periodically repeated microarchitectures, metamaterials deliver many exotic properties beyond those found in natural materials or chemically synthesized substances. After the

pioneering theoretical works on metamaterials over a decade ago [1], experiments first demonstrated the existence of negative permeability and/or negative permittivity in electromagnetic metamaterials [2,3]. Later, optical metamaterials [4,5], acoustic metamaterials [6,7], mechanical metamaterials [8–12] and thermal metamaterials [13,14] triggered a significant amount of research interest in the fields of engineering, physics, material science and chemistry mainly due to their unprecedented and unusual multifunctional properties (e.g. negative refractive index [4,5], negative effective density [6,7], negative incremental stiffness [9], negative Poisson's ratio [10], shape reconfigurability [11], ultra-low density

\* Corresponding author. Department of Bioresource Engineering, McGill University, Island of Montreal, QC, H9X 3V9, Canada.

E-mail address: [hamid.akbarzadeh@mcgill.ca](mailto:hamid.akbarzadeh@mcgill.ca) (A.H. Akbarzadeh).

URL: <https://www.mcgill.ca/bioeng/faculty-and-staff/abdolhamid-akbarzadeh-shafaroudi>

[12], and negative thermal conductivity [14]). If these metamaterials are made of smart materials (e.g. piezoelectric, piezomagnetic, and magnetostrictive materials) in the form of optimized cellular architectures, they can open a new venue for designing lightweight advanced multifunctional materials responsive to arbitrary multiphysical stimuli. Cellular smart metamaterials promise optimized multiphysical properties not readily achievable by existing smart materials. Tailoring the microarchitecture of metamaterials is an effective method to develop optimized multifunctional materials. Rather than merely changing chemical constituents, deliberately optimizing the microarchitecture of smart materials can obtain not inherently achievable multiphysical properties for piezoelectric metamaterials [15,16].

With wide application in ultrasonic imaging devices, sensors, energy harvesting, and transducers, piezoelectric materials have been rapidly developing in recent years. Advanced 3D printing technology [17] and nanotechnology [18] provided reliable routes for manufacturing piezoelectric metamaterials with complex geometries in micro and nano scales. Typically, apart from modifying material constituents, there are two commonly used methods to modify the properties of piezoelectric materials: (1) adding a second phase (piezocomposites) [19–29] and/or (2) introducing pores (cellular piezoelectric materials) [30–40]. Based on the interconnection of the inclusions/pores, there are four types of composite/cellular piezoelectric metamaterials: (1) 0–3 type (inclusions/pores are enclosed by the matrix), (2) 1–3 type (inclusions/pores connect in one direction and matrix connects in all three directions), (3) 2–2 type (both inclusions/pores and matrix exhibit connectivity in two dimensions) and (4) 3–3 type (both inclusions/pores and matrix exhibit connectivity in all three dimensions).

Compared to cellular piezoelectric materials, encapsulating brittle piezoelectric ceramics by soft polymers provides a piezocomposite with excellent electro-mechanical performance. For polymer-based piezocomposites, a piezoelectric matrix (such as Polyvinylidene fluoride (PVDF) [19–21]) showed better figures of merit and piezoelectric properties than a non-piezoelectric matrix (such as epoxy [22–29]). The ceramic-based piezocomposite (such as PZT-7A/BaTiO<sub>3</sub> [19]) was explored to modify the electro-mechanical properties of piezocomposites. Regarding the dimension of inclusion connectivity, 0–3, 1–3 and 2–2 types of piezocomposites with different inclusion shapes and unit cell arrangements were modelled and compared in Ref. [20]. The 0–3 piezocomposites with short piezoelectric fibers (cylinder) [21] and particulate inclusion (sphere) [22] have exhibited similar properties for different volume fractions of inclusion. However, due to their extensive use in biomedical and naval applications, 1–3 piezocomposites attracted more efforts than the other three types of piezocomposites. One method to modify the properties of 1–3 piezocomposites is to engineer the inclusion topology (prismatic inclusion (octagon and square) and non-prismatic inclusion (circle and ellipse) [20]) and unit cell position arrangement (hexagonal and square position arrangement [23]), especially for transversely polarized 1–3 piezocomposite (with polarization direction perpendicular to the inclusion). Another category of 1–3 piezocomposites, such as four-step braided cylindrical inclusions [24], randomly distributed cylindrical inclusions [25], and parallelogram periodic cells [26], have also been investigated to seek the possibility of improving electro-mechanical properties; it was found that changing the position arrangement of unit cells had obvious influence on effective electro-mechanical properties. In addition, functionally graded piezocomposites have been introduced by tailoring polarization direction and material gradation within the smart composites [27]. Compared to 1–3 piezocomposites with circular inclusions, one advantage of 2–2 piezocomposites was its straightforward processing method and avoiding direct connection

between electrodes and piezoelectric phase [28]. One noticeable 2–2 piezocomposites was a Macro Fiber Composite (MFC) with interdigitated electrodes, which has been used as actuators and sensors by a company named as *Smart Material*. In general, 1–3 piezocomposites showed better figures of merit for energy harvesting (higher piezoelectric charge coefficients and coupling constants), while 0–3 piezocomposite revealed the lowest acoustic impedance for biomedical imaging devices. However, the separation of the interface between inclusion and matrix might deteriorate piezocomposites [29].

Introducing pores makes piezoelectric materials brittle; however, cellular piezoelectric metamaterials have shown remarkable improvement in figures of merit, especially for hydrophone applications. Cellular piezoelectric metamaterials can be considered as piezocomposites with empty inclusions, periodically distributed in a piezoelectric matrix [30]. Many studies have recently been conducted to optimize electro-mechanical properties of cellular piezoelectric materials by tailoring their microarchitectures [30–40]. For 0–3 type of cellular piezoelectric metamaterials, alternative pores, e.g. flat-cuboidal, spherical and short-cylindrical, showed different effective electro-mechanical properties; flat-cuboidal pores resulted in better hydrostatic charge and hydrostatic voltage constants [31]. Similar to piezocomposite, electro-mechanical properties of 1–3 cellular piezoelectric materials can be improved by alternative parameters, e.g. pore shape [30], pore aspect ratio [32], and polarization direction [32–35]. For longitudinally polarized porous piezoelectric materials, electro-mechanical properties were insensitive to pore shapes and aspect ratio; opposite behavior has been found for transversely polarized porous piezoelectric materials [30,33–37]. In addition, acoustic impedance and hydrostatic charge constant can be modified by tailoring pore position arrangement [33,34]. As for prismatic pores, auxetic [35], honeycomb [35–37], tetragonal [36,37] and triangular microarchitectures [38,39] have shown different deformation modes and electro-mechanical properties. It was found that along polarization direction, bending dominant deformation mode enhanced the piezoelectric figures of merit. Compared to 1–3 type of piezoelectric cellular materials, 3–3 type of piezoelectric cellular materials have shown great improvement in piezoelectric figures of merit at the cost of deteriorating mechanical performance [38]. Apart from the piezoelectric effect, some pyroelectric figures of merit with cellular microarchitectures also showed obvious improvement compared to that of dense materials [40,41].

In order to obtain the effective properties of architected cellular materials with periodic microarchitectures, both analytical and numerical methods have been proposed. Based on the pioneering work conducted by Eshelby [42], several analytical mean field methods [43–45], e.g. dilute, self-consistent, and Mori–Tanaka, were proposed to predict effective electro-mechanical properties of piezocomposite with alternative inclusion topologies. Among these micromechanical models, Mori–Tanaka micromechanical scheme has provided the most accurate results compared to experimental data. However, local fluctuations of field quantities were not taken into account in these analytical micromechanical models. This restriction can be solved by combination of analytical models with numerical methods, e.g. finite element method. Recently, asymptotic homogenization (analytical method) [23,24,26–28,30,46,47] and finite element method (numerical method) [20,22,25,27,31–37,48] have been widely used to predict the effective properties of cellular materials with periodic microstructures. Although finite element method is straightforward to understand, asymptotic homogenization method has a robust mathematical basis, which provides closed-form expressions for accurate theoretical predictions of effective multiphysical properties of advanced materials with periodic microstructures.

Different 0–3, 1–3, 2–2, 3–3 types of piezoelectric cellular materials have been investigated by analytical (Mori-Tanaka [19,29,33] and asymptotic homogenization [23,24,26,30,31]) and numerical (finite element method [20–22,25,27,32–34,36–38,48]) methods. Employing these methods, some researches have provided the relationship between effective properties and relative density or solid volume fraction. However, the design chart for piezoelectric properties (similar to material selection charts for mechanical properties) yet to be developed to provide a broad view on feasible piezoelectric materials through devising advanced smart materials. In addition, despite of many structural and multifunctional advantages offered by piezocomposites and high figures of merit of lightweight cellular solids, studies on the combination of piezocomposites and cellular solids, i.e. cellular piezocomposite metamaterials, are limited. For example, for cellular piezocomposites made of alternative matrices, it was found that ceramic matrix-based cellular piezocomposites were more sensitive to pores than polymer matrix materials [21]. Based on micromechanical modelling, the introduction of pores to matrix was found to increase the hydrostatic performance of cellular piezocomposites [22]. However, both of the aforementioned researches did not consider the influence of polarization directions and pore shapes on the electromechanical properties. Furthermore, since most of commercial finite element software, e.g. ANSYS and ABAQUS, does not have an appropriate element for pyroelectric constants, investigations on the pyroelectric properties of piezoelectric cellular materials were mostly limited to experimental studies [40,41]. To the best of authors' knowledge, there is no numerical study in the literature on exploring the effect of pore shapes and polarization directions on the effective pyroelectric properties of piezoelectric cellular metamaterials. Therefore, objectives of the present study are:

- To develop an asymptotic homogenization model for characterizing the thermo-electro-mechanical properties (e.g. effective elastic properties, piezoelectric properties, dielectric properties, pyroelectric properties and thermal conductivity) and evaluating the piezoelectric and pyroelectric figures of merit of architected cellular piezoelectric metamaterials.
- To design cellular piezoelectric metamaterials of 1–3 type with alternative pore shapes, polarization directions and non-piezoelectric or piezoelectric phases to optimize the thermo-electro-mechanical properties of cellular smart metamaterials.
- To establish a relation between microarchitectural features and multiphysical properties of piezoelectric metamaterials and to provide a design chart for optimizing their thermo-electro-mechanical properties by tailoring their microarchitecture or material composition.
- To elucidate the rationale for dissimilar thermo-electro-mechanical properties found in longitudinally and transversely polarized cellular metamaterials with and without non-piezoelectric phases.

The present paper is organized as follows: Four types of architected cellular piezoelectric metamaterials are introduced in Section 2. The constitutive and governing equations for uncoupled linear thermo-piezoelectricity are given in Section 3. Section 4 provides details on the implementation of asymptotic homogenization for obtaining the effective thermo-electro-mechanical properties of cellular piezoelectric metamaterials. The role of microarchitectural features of cellular metamaterials on their effective properties and figures of merit are presented in Section 5

compared to conventional honeycomb piezoelectric cellular materials and piezocomposites with solid circular inclusion. To better understand the effect of microarchitecture on thermo-electro-mechanical properties of piezoelectric metamaterials, a detailed discussion is provided in Section 6 on the thermo-electro-mechanical performance of four types of cellular piezoelectric metamaterials. Section 7 highlights the main conclusions extracted from the present study.

## 2. Pore topology of cellular piezoelectric metamaterials

As shown in Fig. 1(a) and (b), according to the polarization direction (axis 3) of constitutive piezoelectric material, 1–3 piezoelectric cellular metamaterials can be further classified as a longitudinally polarized (i.e. polarized along the pore axis) and transversely polarized (i.e. polarized orthogonal to the pore axis) cellular piezoelectric metamaterials. Fig. 1(c) and (d) show a similar metamaterial made of two different materials, whose interface between two materials are assumed to be perfectly bonded. In particular, four types of cellular piezoelectric metamaterials are analyzed in this paper: (1) Longitudinally polarized single material (type I), (2) Transversely polarized single material (type II), (3) Longitudinally polarized bi-material (type III) and (4) Transversely polarized bi-material (type IV).

To better understand the role of microarchitectural features of cellular piezoelectric metamaterials on their effective thermo-electro-mechanical properties, the following Fourier series expansion is used to generate pores of a general two-dimensional (2D) topology [49]:

$$x = r(\omega) \cos\omega, y = r(\omega) \sin\omega$$

where

$$r(\omega) = r_0[1 + c_1 \cos(\alpha\omega) + c_2 \cos(\beta\omega)] \quad (\alpha, \beta = 1, 2, \dots) \quad (1)$$

In Eq. (1),  $\alpha$  and  $\beta$  control symmetry of the pore topology. For example, when  $\alpha = 2$  and  $\beta = 4$ , the pore is two-fold symmetry and when  $\alpha = 3$  and  $\beta = 6$ , the pore is three-fold symmetry. In addition,  $c_1$  and  $c_2$  determine specific pore shapes. Assuming that representative volume element (RVE) of cell is a unit-length square, the solid volume fraction of cellular piezoelectric metamaterials made of a single material is expressed by:

$$f_V = 1 - \frac{\pi(2 + c_1^2 + c_2^2)}{2} r_0^2 \quad (2)$$

where  $f_V$  is solid volume fraction. Similarly, for bi-material cellular piezoelectric metamaterials, matrix ( $f_{Vm}$ ) and inclusion ( $f_{Vi}$ ) volume fractions are expressed by:

$$\begin{aligned} f_{Vm} &= 1 - \frac{\pi(2 + c_1^2 + c_2^2)}{2} r_{0m}^2, \quad f_{Vi} \\ &= \frac{\pi(2 + c_1^2 + c_2^2)}{2} (r_{0m}^2 - r_{0i}^2) \end{aligned} \quad (3)$$

where  $r_{0m}$  and  $r_{0i}$  determine the size of matrix and inclusion, respectively. By rotating ( $\omega_r$  as rotation angle) and scaling ( $s$  as scaling factor or aspect ratio) pores, a wider range of pore microarchitecture can be achieved to further optimize thermo-electro-mechanical properties of cellular piezoelectric metamaterials. The topology of rotated or scaled pores can be determined by the following equations:

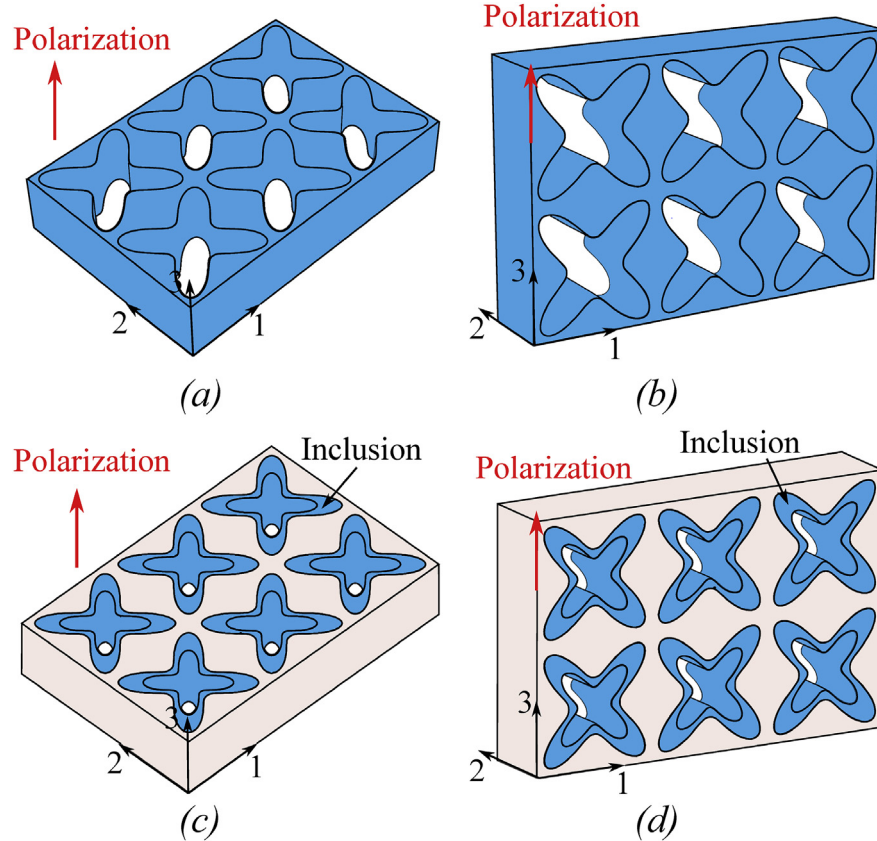


**Fig. 1.** Four types of 1–3 cellular, 2D extruded, piezoelectric metamaterials: (a) Type I (single material with longitudinal polarization); (b) Type II (single material with transverse polarization), (c) Type III (bi-material with longitudinal polarization), and (d) Type IV (bi-material with transverse polarization).

$$\text{Rotating : } x = r(\omega)\cos(\omega + \omega_r), \quad y = r(\omega)\sin(\omega + \omega_r)$$

$$\text{Where } r(\omega) = r_0[1 + c_1 \cos(\alpha\omega) + c_2 \cos(\beta\omega)] \quad \alpha, \beta = 1, 2, \dots$$

$$\text{Scaling : } x = r(\omega)\cos \omega, \quad y = r(\omega)\sin \omega \cdot s$$

$$\text{Where } r(\omega) = r_0[1 + c_1 \cos(\alpha\omega) + c_2 \cos(\beta\omega)]/s \quad \alpha, \beta = 1, 2, \dots$$

According to Eqs. (1) and (4), Fig. 2(a) presents 25 different shapes of four-fold symmetrical pores with  $\alpha = 4, \beta = 8, \omega_r = 0, s = 1$  and  $f_V = 0.8$ , while  $c_1$  and  $c_2$  vary between -0.4 and 0.4 to show their effect on pore topology. Fig. 2(b) scales down ( $s = 2$ ) and rotates ( $\omega_r = 45^\circ$  counter-clockwise) pores presented in Fig. 2(a). Fig. 2(c) shows three-fold symmetrical pores with  $\alpha = 3, \beta = 6, s = 1, \omega_r = 0$  and  $f_V = 0.8$  to reveal how shape parameters  $\alpha$  and  $\beta$  can tailor the pore microarchitecture in cellular metamaterials. In Fig. 2(b), it can be seen that although neither  $x$  axis nor  $y$  axis is symmetry axis of these pores, these pores still have four-fold symmetry. The bi-material cellular microarchitectures are shown in Fig. 2(d) for matrix and inclusion volume fractions of  $f_{Vm} = 0.6$  and  $f_{Vi} = 0.3$ ; both piezoelectric inclusions (blue area) and pores share the same topology. It should be mentioned that when piezoelectric inclusion boundary touches the unit cell or RVE boundary (e.g. for  $c_1 = c_2 = 0.4$  in Fig. 2 (d)), we call this topology an

inadmissible geometry since it makes the matrix unconnected. To showcase the unprecedented thermo-electro-mechanical properties of architected cellular piezoelectric metamaterials, we compare their effective properties with conventional 2D extruded piezoelectric honeycombs or piezocomposites with solid circular inclusion. In the following sections, we use a computational approach based on AH to theoretically predict the effect of pore topology, polarization direction and material composition on the thermo-electro-mechanical properties of cellular piezoelectric metamaterials.

### 3. Constitutive and governing equations of piezoelectric materials

The constitutive equations of thermo-piezoelectric materials are derived by applying the principle of free energy. The Helmholtz free energy,  $F$ , can be written as follows [50,51].

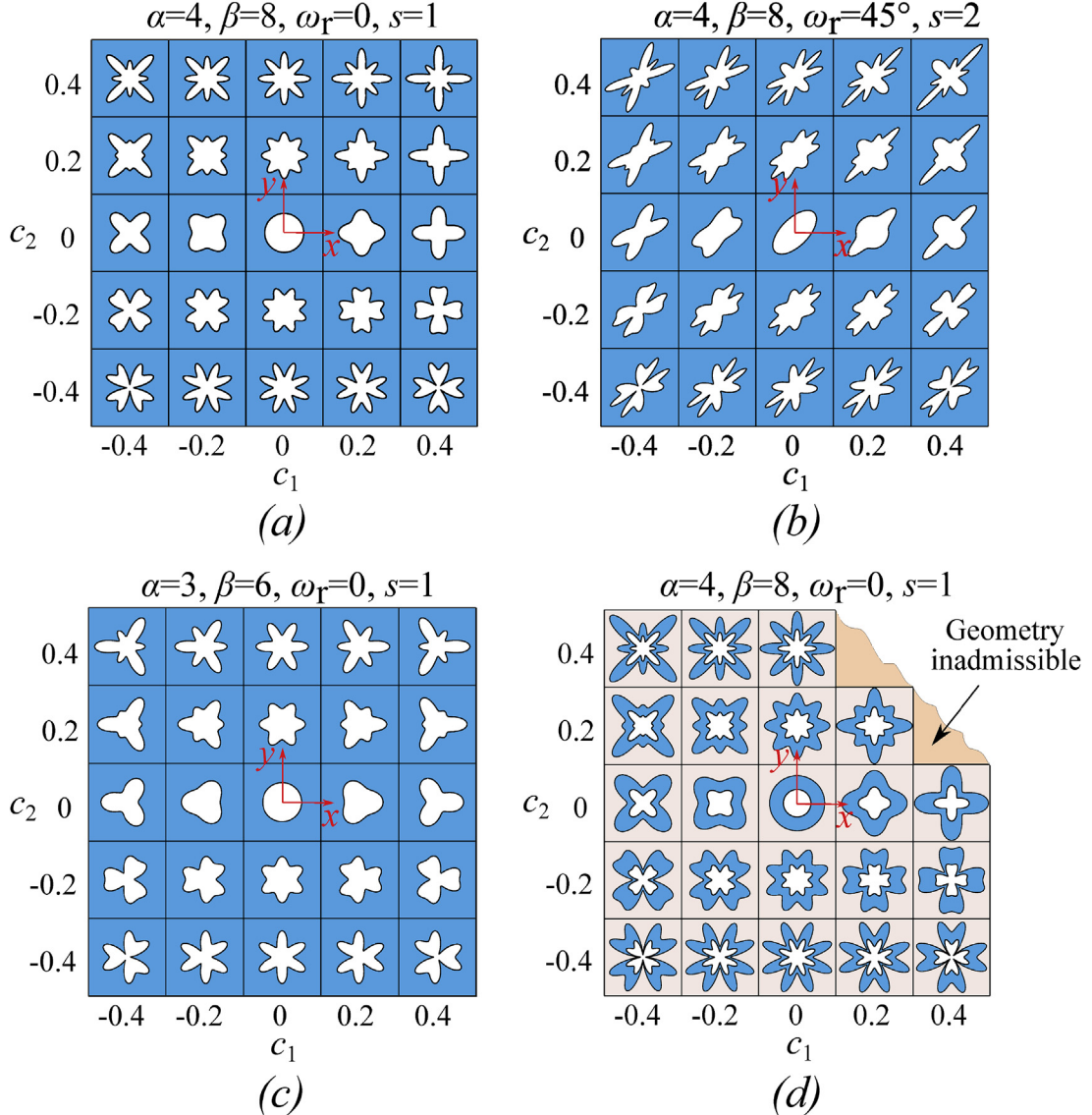


**Fig. 2.** Cross section of 1–3 cellular, 2D extruded, piezoelectric metamaterials: (a) Single material with  $\alpha = 4$ ,  $\beta = 8$ ,  $\theta_r = 0$  and  $s = 1$ , (b) Single material with  $\alpha = 4$ ,  $\beta = 8$ ,  $\theta_r = 45^\circ$  and  $s = 1$ , (c) Single material with  $\alpha = 3$ ,  $\beta = 6$ ,  $\theta_r = 0$  and  $s = 1$ , and (d) Bi-material with  $f_{vm} = 0.6$ ,  $f_{vi} = 0.3$ ,  $\alpha = 4$ ,  $\beta = 8$ ,  $\theta_r = 0$  and  $s = 1$ .

$$\begin{aligned} F(\epsilon_{ij}, E_i, \theta) &= \frac{1}{2} \epsilon_{ij} C_{ijkl} \epsilon_{kl} - e_{ijk} E_i \epsilon_{jk} - \frac{1}{2} \kappa_{ij} E_i E_j - \lambda_{ij} \theta \epsilon_{ij} \\ &\quad + p_i E_i \theta - \frac{1}{2} c_T \theta^2 \end{aligned} \quad (5)$$

where  $\epsilon_{ij}$ ,  $E_i$  and  $\theta$  ( $i, j, k, l = 1, 2, 3$ ) are strain tensor, electric field vector and temperature difference changing from reference temperature, respectively;  $C_{ijkl}$ ,  $e_{ijk}$ ,  $\kappa_{ij}$ ,  $\lambda_{ij}$  and  $p_i$  are respectively, elastic, piezoelectric, dielectric, thermal-stress and primary pyroelectric coefficient vectors;  $c_T$  is volumetric heat capacity and defined as  $c_T = c_E / \theta_0$ , where  $c_E$  is heat capacity and  $\theta_0$  is initial temperature.

Piezoelectric materials with linear constitutive relations are considered in the present work. This implies constant material constants and the constitutive relations as:

$$\sigma_{ij} = \frac{\partial F}{\partial \epsilon_{ij}} = C_{ijkl} \epsilon_{ij} - e_{ijk} E_k - \lambda_{ij} \theta \quad (6a)$$

$$D_i = -\frac{\partial F}{\partial E_i} = e_{ijk} \epsilon_{jk} + \kappa_{ij} E_j - p_i \theta \quad (6b)$$

$$S = -\frac{\partial F}{\partial \theta} = \lambda_{ij} \epsilon_{ij} + p_i E_i + c_T \theta \quad (6c)$$

where  $\sigma_{ij}$ ,  $D_i$  and  $S$  ( $i, j = 1, 2, 3$ ) are stress tensor, electric displacement vector and entropy, respectively. For a reversible process,  $S$  can be derived from the second law of thermodynamics as:

$$dS = \frac{dQ}{\theta} \quad (7)$$

where  $Q$  is the absorbed heat.

Neglecting body force and volume charges, governing equations for the thermopiezoelectricity problems are [52–55]:

$$\sigma_{ij,j} = \rho \ddot{u}_i \quad (8a)$$

$$D_{i,i} = 0 \quad (8b)$$

$$\rho(\theta\dot{S} - R) + q_{i,i} = 0 \quad (8c)$$

where  $\rho$  is density,  $u_i$  is displacement vector and  $R$  is the heat produced per unit time and unit mass and  $q_i$  is heat flux per unit area and per unit time; overdot means derivative with respect to time. Combining Eq. (8c) and Fourier's law for heat conduction (Eq. (A.1)), the relationship between temperature and entropy can be written as:

$$\rho(\theta\dot{S} - R) + (K_{ij}\theta_j)_j = 0 \quad (9)$$

where  $K_{ij}$  is thermal conductivity.

Based on Eq. (9), for stationary linear thermo-electro-mechanical fields,  $\dot{S} = 0$  and entropy does not have any influence on temperature field, while temperature can indirectly affect entropy (Eq. (6c)). The multiphysical relation among this partially coupled stationary thermo-electro-mechanical fields is presented in Fig. 3.

As shown in Fig. 3, electric and mechanical fields are fully coupled by the piezoelectric/inverse piezoelectric effect; temperature affects the electric field/displacement and strain/stress by pyroelectric effect and thermal expansion/stress coefficient, respectively. In addition, electric field and electric displacement have mutual influence on each other; it is the same for strain and stress. Although temperature can affect electric and mechanical fields and both electric and mechanical fields have influence on entropy, the variation of entropy has no influence on temperature for stationary or steady-state conditions. Therefore, for stationary linear thermo-piezoelectric fields, it is reasonable to keep the temperature field uncoupled from the mechanical/electrical fields. Herein, the effective thermo-piezoelectric properties are obtained for stationary linear thermo-electro-mechanical field [19–39,42–48,54]. Therefore, we assume mechanical and electric

fields are coupled while temperature field is not affected by the mechanical and electric fields; such analysis is so-called uncoupled thermo-piezoelectricity [53–55]. For transient coupled thermo-piezoelectricity analysis, such as those considered in Ref. [56], the effective properties obtained by stationary conditions is still used but Eqs. (6c) and (8c) should be considered for solving the governing equations in time domain.

In linear piezoelectricity, strain tensor and electric field vector are related to mechanical displacement  $u_k$  and electric potential  $\phi$  as:

$$\varepsilon_{kl} = \frac{1}{2} \left( \frac{\partial u_k}{\partial x_l} + \frac{\partial u_l}{\partial x_k} \right), \quad E_k = -\frac{\partial \phi}{\partial x_k} \quad (10)$$

The thermo-piezoelectric constants mentioned in Eq. (6) are defined as:

$C = (\partial\sigma/\partial\varepsilon)_{E,\theta}$ : Elastic tensor measured at constant electric field and temperature

$e = (\partial D/\partial\varepsilon)_{E,\theta} = (-\partial\sigma/\partial E)_{\varepsilon,\theta}^T$ : Piezoelectric tensor measured at constant electric field and temperature or at constant strain and temperature

$\kappa = (\partial D/\partial E)_{\varepsilon,\theta}$ : Dielectric permittivity tensor measured at constant strain and temperature

$\lambda = (\partial\sigma/\partial\theta)_{\varepsilon,E}$ : Thermal stress tensor measured at constant strain and electric fields

$p = (\partial D/\partial\theta)_{\varepsilon,E}$ : Pyroelectric tensor measured at constant strain and electric fields

In this paper, bold symbols are used for tensors or matrix and bold italic symbols stand for vectors, superscript T denotes transposition, and the subscripts following the partial derivatives indicate the fields are constant during the measurement of the thermo-piezoelectric moduli.

The aforementioned fourth-ranked elastic tensor and third-ranked piezoelectric tensor can be simplified with Voigt notation, which uses the following mapping of adjacent indices:  $11 \rightarrow 1$ ,

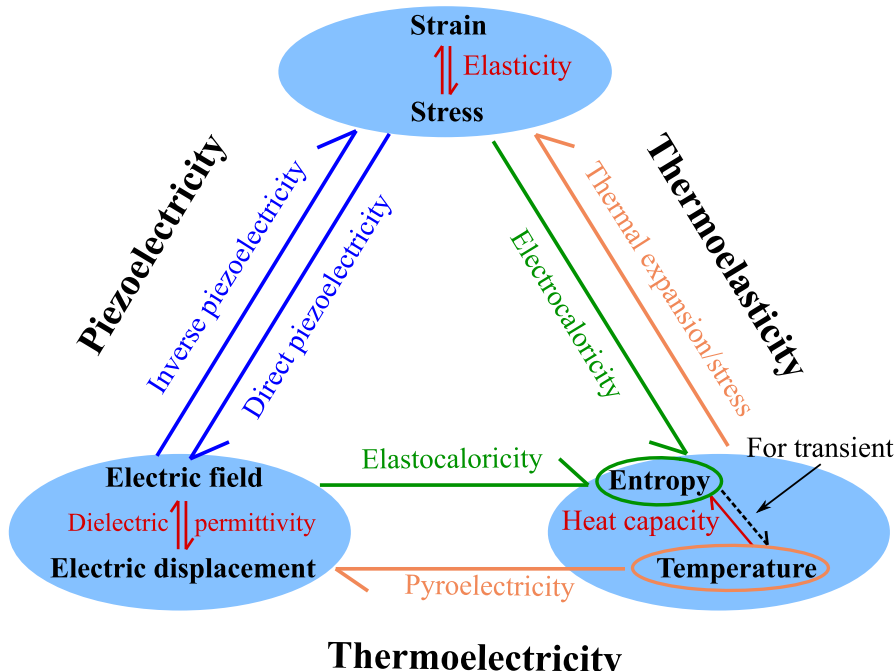


Fig. 3. Partly coupled stationary thermo-piezoelectric fields.

$22 \rightarrow 2$ ,  $33 \rightarrow 3$ ,  $23 \rightarrow 4$ ,  $13 \rightarrow 5$ ,  $12 \rightarrow 6$ . Correspondingly, Eq. (6) can be rewritten in a compact form as:

$$\mathbf{E} = \mathbf{EZ} - \Pi\theta \quad (11)$$

where  $\Sigma = (\sigma_1 \sigma_2 \sigma_3 \sigma_4 \sigma_5 \sigma_6 D_1 D_2 D_3)^T$ ,  $\mathbf{Z} = (e_1 e_2 e_3 e_4 e_5 e_6 E_1 E_2 E_3)^T$ ,  $\Pi = (\lambda_1 \lambda_2 \lambda_3 \lambda_4 \lambda_5 \lambda_6 p_1 p_2 p_3)^T$  and

$$\mathbf{E} = \begin{bmatrix} C_{11} & C_{12} & C_{13} & C_{14} & C_{15} & C_{16} & e_{11} & e_{12} & e_{13} \\ \cdot & C_{22} & C_{23} & C_{24} & C_{25} & C_{26} & e_{21} & e_{22} & e_{23} \\ \cdot & \cdot & C_{33} & C_{34} & C_{35} & C_{36} & e_{31} & e_{32} & e_{33} \\ \cdot & \cdot & \cdot & C_{44} & C_{45} & C_{46} & e_{41} & e_{42} & e_{43} \\ \cdot & \cdot & \cdot & \cdot & C_{55} & C_{56} & e_{51} & e_{52} & e_{53} \\ \cdot & \cdot & \cdot & \cdot & \cdot & C_{66} & e_{61} & e_{62} & e_{63} \\ e_{11} & e_{21} & e_{31} & e_{41} & e_{51} & e_{61} & -\kappa_{11} & -\kappa_{21} & -\kappa_{31} \\ e_{21} & e_{22} & e_{23} & e_{24} & e_{25} & e_{26} & \cdot & -\kappa_{22} & -\kappa_{23} \\ e_{31} & e_{32} & e_{33} & e_{34} & e_{35} & e_{36} & \cdot & \cdot & -\kappa_{33} \end{bmatrix} \quad (12)$$

In Eq. (12),  $(\cdot)$  represents symmetric elastic, piezoelectric and dielectric coefficients about the main diagonal of  $\mathbf{E}$  matrix. Therefore, 54 material constants (21 elastic, 18 piezoelectric, 6 permittivity, 6 thermal stress and 3 primary pyroelectric constants) are needed to describe the properties of the thermo-piezoelectric materials. In order to give more thermal related properties, for the analysis below, the common alternative form of thermal related coefficients, i.e. thermal expansion coefficients  $\Delta_{ij}$  and total pyroelectric coefficients  $\gamma_i$ , are also used which are calculated by Ref. [51]:

$$\Lambda = \mathbf{E}^{-1}\Pi \quad (13)$$

where  $\Lambda = (\Delta_{11} \Delta_{22} \Delta_{33} \Delta_{23} \Delta_{13} \Delta_{12} \gamma_1 \gamma_2 \gamma_3)^T$ .

The governing equations of the thermo-piezoelectric materials are defined as [55]:

$$\nabla \cdot \boldsymbol{\sigma} + \mathbf{b} = 0 \quad (14a)$$

$$\nabla \cdot \mathbf{D} - q = 0 \quad (14b)$$

$$\nabla \cdot \mathbf{q} - R = 0 \quad (14c)$$

where  $\mathbf{b}$  are body force,  $q$  is free charge, and  $\mathbf{q}$  is heat flux vector.

In order to assess the performance of devices made of piezoelectric materials, four figures of merit for piezoelectric applications (i.e. piezoelectric coupling constant ( $k_t$ ), acoustic impedance ( $Z$ ), piezoelectric charge coefficient ( $d_h$ ) and hydrostatic figure of merit ( $d_h \times g_h$ )) and three figures of merit for pyroelectric applications (i.e. current responsivity ( $F_I$ ), voltage responsivity ( $F_V$ ) and pyroelectric energy harvesting figure of merit ( $F'_E$ )) are discussed [38,57].

**Piezoelectric coupling constant:** The piezoelectric coupling constant,  $k_t = (1 - C_{33}/C_{33}^D)^{0.5}$ , describes the efficiency of energy conversion between electric and mechanical domain. For energy harvesting and biomedical imaging applications, higher  $k_t$  is desirable.

**Acoustic impedance:** The acoustic impedance,  $Z = (\bar{\rho}C_{33}^D)^{0.5}$ , represents the overall acoustic load at the interface between a device (e.g., hydrophone) and its surrounding aqueous environment, where  $\bar{\rho}$  is effective density and  $C_{33}^D = C_{33} + (e_{33})^2/\kappa_{33}$ . For underwater acoustic transducer or hydrophones, lower  $Z$  means better performance.

**Hydrostatic charge coefficient:** The hydrostatic (or piezoelectric) charge coefficient,  $d_h = d_{33} + d_{31} + d_{32}$ , assesses the conversion of mechanical loads (under hydrostatic loading) to electric signals.

Therefore, higher  $d_h$  will enhance hydrophone device sensitivity to detect sound. It should be mentioned that the piezoelectric strain coefficient ( $d_{nlk}$ ) is related to the piezoelectric coefficient ( $e_{nij}$ ) as:  $e_{nij} = d_{nlk} \cdot C_{klj}$ .

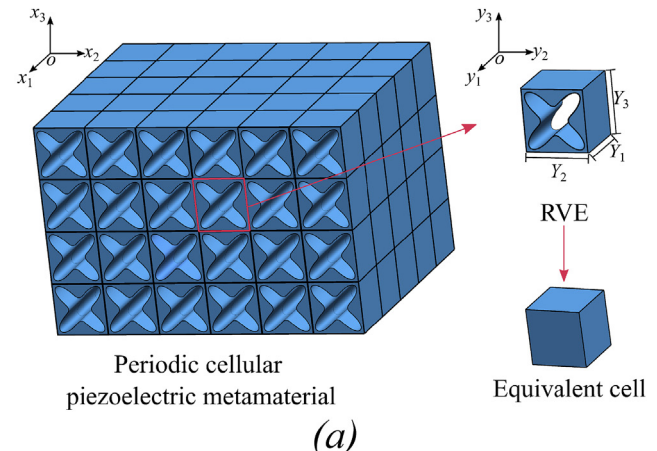
**Hydrostatic figure of merit:** The hydrostatic figure of merit,  $d_h \times g_h$ , defines the ability of a hydrophone device to identify and distinguish a signal from the ambient background noise. Here, the hydrostatic voltage coefficient,  $g_h$ , is given by  $d_h/\kappa_{33}^\sigma$ , where  $\kappa^\sigma = \kappa + e^T C^{-1} e$ , and larger  $d_h \times g_h$  means higher signal-to-noise ratio.

**Voltage responsivity and Current responsivity:** For heat and infrared (IR) detection, which is based on the generation of maximum current or voltage for a given thermal energy input, higher voltage responsivity ( $F_I$ ) and current responsivity ( $F_V$ ) improve the device sensitivity:

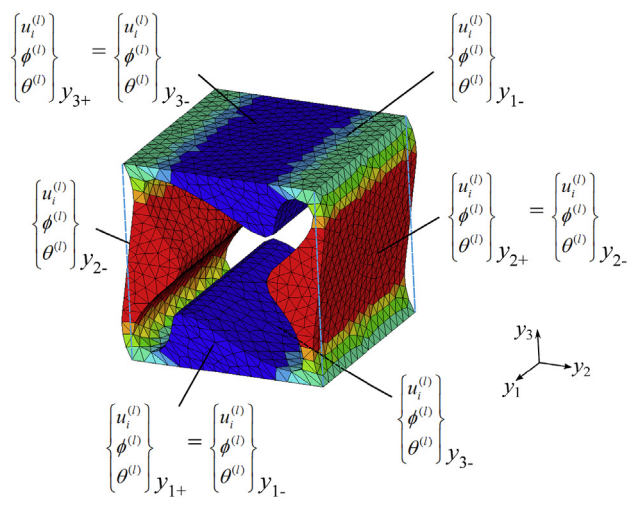
$$F_I = \frac{p_3}{c_E} = \frac{p_3}{\rho \cdot c_p}, \quad F_V = \frac{p_3}{c_E \cdot \kappa_{33}^\sigma} = \frac{p_3}{\rho \cdot c_p \cdot \kappa_{33}^\sigma} \quad (15)$$

where  $c_p$  is specific heat capacity.

**Pyroelectric energy harvesting figure of merit:** The pyroelectric energy harvesting figure of merit,  $F'_E$ , indicates the thermal energy density generated by a given thermal input which can be seen as the product of  $F_I$  and  $F_V$ , namely:



(a)  
Periodic cellular  
piezoelectric metamaterial  
Equivalent cell



(b)  
Fig. 4. Schematic figure of (a) Homogenization process and (b) Periodic boundary conditions.

$$F'_E = \frac{p_3^2}{c_E^2 \cdot K_{33}^\sigma} \quad (16)$$

#### 4. Asymptotic homogenization for thermo-electro-mechanical properties of cellular piezoelectric metamaterials

Cellular piezoelectric metamaterials are considered as advanced periodic structural elements with optimized multifunctional properties, commonly used for application in meso and macro scales. However, detailed numerical simulation of structures made of many cells of piezoelectric metamaterials is a cumbersome task since it is expensive computationally. One of the most efficient approaches for predicting the overall multiphysical properties of heterogeneous advanced architected materials with engineered microstructures is to analyze their representative volume elements (RVE) (see Fig. 4(a)) and obtain a macroscopic homogenous medium equivalent to the original heterogeneous microstructure using homogenization techniques [46,47]. Two widely adopted homogenization techniques are: asymptotic homogenization (AH) and standard method (SM) or so-called finite element method. In this paper, AH is used to predict the effective thermo-electro-mechanical properties of the architected cellular piezoelectric metamaterials presented in Section 2. In contrast to SM homogenization, AH has a well-developed mathematical foundation which enables to extend this multiscale homogenisation technique to other coupled multiphysical fields.

As shown in Fig. 4(a), there are two distinct scales in this periodic structures. The first one is the macroscopic scale with a coordinate of  $\{O, x_1, x_2, x_3\}$  and the other one is the microscopic scale with a coordinate of  $\{O, y_1, y_2, y_3\}$ ;  $\eta (\ll 1)$  is a magnification factor and  $y_i = x_i/\eta$ . In microscopic coordinate, RVE is  $\mathbf{Y}$ -periodic with  $\mathbf{Y} = (Y_1, Y_2, Y_3)$ . Based on asymptotic expansion in powers of macroscopic scale  $x$  and microscopic scale  $y$ , thermo-electro-mechanical fields can be determined by:

where superscript  $^{**}$  represents dependency on the RVE size of inhomogeneity;  $u_i^{(l)}, \phi^{(l)}, \theta^{(l)}$  are  $\mathbf{Y}$ -periodic with respect to the microscopic coordinate. Therefore, in Fig. 4(b), the displacement, voltage and temperature in two opposite faces are the same. In addition, within the same material, the stiffness tensor  $\mathbf{C}^*$ , piezoelectric tensor  $\mathbf{e}^*$ , dielectric permittivity tensor  $\kappa^*$ , thermal stress tensor  $\lambda^*$  and pyroelectric tensor  $\mathbf{p}^*$  are also  $\mathbf{Y}$ -periodic but independent of macroscopic scale, namely  $\mathbf{C}^*(\mathbf{x}, \mathbf{y}) = \mathbf{C}(\mathbf{y})$ ,  $\mathbf{e}^*(\mathbf{x}, \mathbf{y}) = \mathbf{e}(\mathbf{y})$ ,  $\kappa^*(\mathbf{x}, \mathbf{y}) = \kappa(\mathbf{y})$ ,  $\lambda^*(\mathbf{x}, \mathbf{y}) = \lambda(\mathbf{y})$  and  $\mathbf{p}^*(\mathbf{x}, \mathbf{y}) = \mathbf{p}(\mathbf{y})$ . Based on chain rule and relationship between macroscopic and microscopic scales, we can write:

$$\frac{\partial}{\partial x_i} \rightarrow \frac{\partial}{\partial x_i} + \frac{1}{\eta} \frac{\partial}{\partial y_i} = \frac{\partial}{\partial x_i} + \frac{1}{\eta} (\cdot)_{,i} \quad (18)$$

Due to the arbitrary value of  $\eta$ , after substituting Eqs. (18) and (17) into Eq. (14a), the governing differential equation of the mechanical field can be expanded and rearranged with the same order of  $\eta$  as:

$$\eta^{-2} : \quad \left( C_{ijkl}^* u_{k,l}^{(0)} \right)_j + \left( e_{ijk}^* \phi_{,k}^{(0)} \right)_j = 0 \quad (19a)$$

$$\begin{aligned} \eta^{-1} : & \left[ C_{ijkl}^* \left( \frac{\partial u_k^{(0)}}{\partial x_l} + u_{k,l}^{(1)} \right) \right]_j + \frac{\partial}{\partial x_j} \left( C_{ijkl}^* u_{k,l}^{(0)} \right) \\ & + \left[ e_{ijk}^* \left( \frac{\partial \phi^{(0)}}{\partial x_k} + \phi_{,k}^{(1)} \right) \right]_j + \frac{\partial}{\partial x_j} \left( e_{ijk}^* \phi_{,k}^{(0)} \right) - \left( \lambda_{ij} \theta^{(0)} \right)_j \\ & = 0 \end{aligned} \quad (19b)$$

$$\begin{aligned} u_i^* &= u_i \left( \mathbf{x}, \mathbf{y} = \frac{\mathbf{x}}{\eta} \right) = \sum_{l=0}^{+\infty} \eta^l u_i^{(l)}(\mathbf{x}, \mathbf{y}) = u_i^{(0)}(\mathbf{x}, \mathbf{y}) + \eta u_i^{(1)}(\mathbf{x}, \mathbf{y}) + O(\eta^2) \\ \phi^* &= \phi \left( \mathbf{x}, \mathbf{y} = \frac{\mathbf{x}}{\eta} \right) = \sum_{l=0}^{+\infty} \eta^l \phi^{(l)}(\mathbf{x}, \mathbf{y}) = \phi^{(0)}(\mathbf{x}, \mathbf{y}) + \eta \phi^{(1)}(\mathbf{x}, \mathbf{y}) + O(\eta^2) \\ \theta^* &= \theta \left( \mathbf{x}, \mathbf{y} = \frac{\mathbf{x}}{\eta} \right) = \sum_{l=0}^{+\infty} \eta^l \theta^{(l)}(\mathbf{x}, \mathbf{y}) = \theta^{(0)}(\mathbf{x}, \mathbf{y}) + \eta \theta^{(1)}(\mathbf{x}, \mathbf{y}) + O(\eta^2) \end{aligned} \quad (17)$$

$$\begin{aligned} \eta^0 : & \left[ C_{ijkl}^* \left( \frac{\partial u_k^{(1)}}{\partial x_l} + u_{k,l}^{(2)} \right) \right]_j + \frac{\partial}{\partial x_j} \left[ C_{ijkl}^* \left( \frac{\partial u_k^{(0)}}{\partial x_l} + u_{k,l}^{(1)} \right) \right] + \left[ e_{ijk}^* \left( \frac{\partial \phi^{(1)}}{\partial x_k} + \phi_{,k}^{(2)} \right) \right]_j + \\ & \frac{\partial}{\partial x_j} \left[ e_{ijk}^* \left( \frac{\partial \phi^{(0)}}{\partial x_k} + \phi_{,k}^{(1)} \right) \right] - \lambda_{ij} \frac{\partial \theta^{(0)}}{\partial x_j} - \left( \lambda_{ij} \theta^{(1)} \right)_j + b_i = 0 \end{aligned} \quad (19c)$$

Analogously, the following three equations can be extracted from Eq. (14b):

$$\eta^{-2} : \left( e_{ikl}^* u_{k,l}^{(0)} \right)_i - \left( \kappa_{il}^* \phi_{,l}^{(0)} \right)_i = 0 \quad (20a)$$

$$\begin{aligned} \eta^{-1} : & \left[ e_{ikl}^* \left( \frac{\partial u_k^{(0)}}{\partial x_l} + u_{k,l}^{(1)} \right) \right]_i + \frac{\partial}{\partial x_i} \left( e_{ikl}^* u_{k,l}^{(0)} \right) \\ & - \left[ \kappa_{il}^* \left( \frac{\partial \phi^{(0)}}{\partial x_l} + \phi_{,l}^{(1)} \right) \right]_i - \frac{\partial}{\partial x_i} \left( \kappa_{il}^* \phi_{,l}^{(0)} \right) - \left( p_i \theta^{(0)} \right)_i \\ & = 0 \end{aligned} \quad (20b)$$

$$\begin{aligned} \eta^0 : & \left[ e_{ikl}^* \left( \frac{\partial u_k^{(1)}}{\partial x_l} + u_{k,l}^{(2)} \right) \right]_i + \frac{\partial}{\partial x_i} \left[ e_{ikl}^* \left( \frac{\partial u_k^{(0)}}{\partial x_l} + u_{k,l}^{(1)} \right) \right] - \left[ \kappa_{il}^* \left( \frac{\partial \phi^{(1)}}{\partial x_l} + \phi_{,l}^{(2)} \right) \right]_i \\ & - \frac{\partial}{\partial x_i} \left[ \kappa_{il}^* \left( \frac{\partial \phi^{(0)}}{\partial x_l} + \phi_{,l}^{(1)} \right) \right] - p_i \frac{\partial \theta^{(0)}}{\partial x_i} - \left( p_i \theta^{(1)} \right)_i - q = 0 \end{aligned} \quad (20c)$$

In Eqs. (19a) and (20a), only mechanical and electric fields are involved. Referring to the governing equations of coupled fields in a thermo-piezoelectric medium (Eq. (14)),  $u_i^{(0)}$  and  $\phi^{(0)}$  are displacement and electric potentials of the coupled electro-mechanical fields within RVE without any applied force and electric field. Therefore,  $u_i^{(0)}$  and  $\phi^{(0)}$  remain constant in the microscopic scale and only depend on the macroscopic scale:

$$u_i^{(0)}(\mathbf{x}, \mathbf{y}) = U_i(\mathbf{x}) \text{ and } \phi^{(0)}(\mathbf{x}, \mathbf{y}) = \Phi(\mathbf{x}) \quad (21)$$

Similarly, in temperature field,  $\theta^{(0)}$  is also the macroscopic temperature and

$$\theta^{(0)}(\mathbf{x}, \mathbf{y}) = \Theta(\mathbf{x}) \quad (22)$$

Based on Eqs. (21) and (22), Eqs. (19b) and (20b) can be rewritten at the order of  $\eta^{-1}$ :

$$\begin{aligned} \left( C_{ijkl}^* u_{k,l}^{(1)} \right)_j + C_{ijkl,j}^* \frac{\partial U_k}{\partial x_l} + \left( e_{kij}^* \phi_{,k}^{(1)} \right)_j + e_{ijk,j}^* \frac{\partial \Phi}{\partial x_k} - \left( \lambda_{ij} \theta^{(0)} \right)_j &= 0 \\ \left( e_{ikl}^* u_{k,l}^{(1)} \right)_i + e_{ikl,i}^* \frac{\partial U_k}{\partial x_l} - \left( \kappa_{il}^* \phi_{,l}^{(1)} \right)_i - \kappa_{il,i}^* \frac{\partial \Phi}{\partial x_l} - \left( p_i \theta^{(0)} \right)_i &= 0 \end{aligned} \quad (23)$$

In Eq. (23), the first-order terms  $u_i^{(1)}$  and  $\phi^{(1)}$  represent the microscale fluctuations in mechanical displacement and electric potential and are related to macroscopic temperature change  $\Theta$ , mechanical displacement  $U_i$ , and electric potential  $\Phi$  as:

$$\begin{aligned} u_k^{(1)}(\mathbf{x}, \mathbf{y}) &= M U_k^{mn}(\mathbf{y}) \frac{\partial U_m(\mathbf{x})}{\partial x_n} + M \Phi_k^n(\mathbf{y}) \frac{\partial \Phi(\mathbf{x})}{\partial x_n} + M \Theta_k(\mathbf{y}) \Theta(\mathbf{x}) \\ \phi^{(1)}(\mathbf{x}, \mathbf{y}) &= N U_k^{mn}(\mathbf{y}) \frac{\partial U_m(\mathbf{x})}{\partial x_n} + N \Phi_k^n(\mathbf{y}) \frac{\partial \Phi(\mathbf{x})}{\partial x_n} + N \Theta(\mathbf{y}) \Theta(\mathbf{x}) \end{aligned} \quad (24)$$

where  $m, n = 1, 2, 3$  and these six kinds of functions  $M U_k^{mn}$ ,  $M \Phi_k^n$ ,  $M \Theta_k$ ,  $N U_k^{mn}$ ,  $N \Phi_k^n$  and  $N \Theta$  depend only on the microscopic scale. It

should be mentioned that since  $u_k^{(1)}(\mathbf{x}, \mathbf{y})$  and  $\phi^{(1)}(\mathbf{x}, \mathbf{y})$  are  $\mathbf{Y}$ -periodic functions,  $M U_k^{mn}$ ,  $M \Phi_k^n$ ,  $M \Theta_k$ ,  $N U_k^{mn}$ ,  $N \Phi_k^n$  and  $N \Theta$  are also periodic. For AH method, an important step is to obtain these six kinds of functions to express microscale fluctuation terms ( $u_k^{(1)}(\mathbf{x}, \mathbf{y})$  and  $\phi^{(1)}(\mathbf{x}, \mathbf{y})$ ) by the macroscopic field ( $U_i$ ,  $\Phi$  and  $\Theta$ ). Inserting Eq. (24) into Eq. (23) and rearranging these terms based on the derivation of the macroscopic field, three kinds of differential equation sets can be obtained. Since these three kinds of differential equations are only related to RVE, they are also called local problems and the aforementioned six unknown functions are the solutions of these local problems. In particular,  $M U_k^{mn}$  and  $N U_k^{mn}$  are the solutions of the following local mechanical problem:

$$\begin{cases} e_{ikl}^* M U_k^{mn} - \kappa_{il}^* N U_{,l}^{mn} + e_{mni}^* = 0 \\ C_{ijkl}^* M U_k^{mn} + e_{kij}^* N U_{,k}^{mn} + C_{ijmn}^* = 0 \quad \|M U_k^{mn}\| = 0 \quad \text{on } S \\ \|N U_k^{mn}\| = 0 \quad \text{on } S \end{cases} \quad (25)$$

where double bar notation  $\|f\|$  denotes the difference of function  $f$  between two opposite faces  $S$ , i.e.  $\|f\| = f_{y_{1+}} - f_{y_{1-}}$ , which guarantees the periodicity of the solution. In addition, for bi-material RVE,  $S$  includes the interface between the two different materials.

Similarly,  $M \Phi_k^n$  and  $N \Phi_k^n$  are determined by the following local electrical problem:

$$\begin{cases} e_{ikl}^* M \Phi_{k,l}^n - \kappa_{il}^* N \Phi_{,l}^n - \kappa_{in}^* = 0 \\ C_{ijkl}^* M \Phi_{k,l}^n + e_{kij}^* N \Phi_{,k}^n + e_{ijn}^* = 0 \quad \|M \Phi_k^n\| = 0 \quad \text{on } S \\ \|N \Phi_k^n\| = 0 \quad \text{on } S \end{cases} \quad (26)$$

and  $M \Theta_k$  and  $N \Theta$  are defined by the following local thermal problem:

$$\begin{cases} e_{ikl}^* M \Theta_{k,l} - \kappa_{il}^* N \Theta_{,l} - p_i = 0 \\ C_{ijkl}^* M \Theta_{k,l} + e_{kij}^* N \Theta_{,k} - \lambda_{ij} = 0 \quad \|M \Theta\| = 0 \quad \text{on } S \\ \|N \Theta\| = 0 \quad \text{on } S \end{cases} \quad (27)$$

In most available commercial software, the pyroelectric parameters,  $p_i$ , are not provided. Therefore, a code is written in MATLAB to solve the aforementioned local problems. Detailed formulations of the finite element model for solving the local

problems within the thermo-piezoelectric medium are given in Appendix A and the solution of these local problems are provided in Appendix B.

In the order of  $\eta^0$ , substituting Eq. (24) into Eqs. (19c) and (20c) and integrating it over the RVE, considering the Y-periodicity of  $u_k^{(2)}$  and  $\phi^{(2)}$ , the following macroscopic constitutive equations are obtained:

$$\begin{aligned} & \left\langle C_{ijmn}^* + C_{ijkl}^* M U_{k,l}^{mn} + e_{ijl}^* N U_{l,m}^{mn} \right\rangle \frac{\partial^2 U_m}{\partial x_j \partial x_n} + \left\langle e_{ijn}^* + C_{ijkl}^* M \Phi_{k,l}^n + e_{ijl}^* N \Phi_{l,m}^n \right\rangle \frac{\partial^2 \Phi}{\partial x_j \partial x_n} - \\ & \left\langle \lambda_{ij}^* - C_{ijkl}^* M \Theta_{k,l} - e_{ijl}^* N \Theta_{l,m} \right\rangle \frac{\partial \Theta}{\partial x_j} + b_i = 0 \end{aligned} \quad (28a)$$

$$\begin{aligned} & \left\langle e_{imn}^* + e_{ikl}^* M U_{k,l}^{mn} - \kappa_{in}^* N U_{l,m}^{mn} \right\rangle \frac{\partial^2 U_m}{\partial x_i \partial x_n} - \left\langle \kappa_{in}^* - e_{ikl}^* M \Phi_{k,l}^n + \kappa_{il}^* N \Phi_{l,m}^n \right\rangle \frac{\partial^2 \Phi}{\partial x_i \partial x_n} - \\ & \left\langle p_i^* - e_{ikl}^* M \Theta_{k,l} - \kappa_{il}^* N \Theta_{l,m} \right\rangle \frac{\partial \Theta}{\partial x_i} - q = 0 \end{aligned} \quad (28b)$$

where  $\langle(\cdot)\rangle = \frac{1}{V_Q} \int_Q (\cdot) dV$  and  $V_Q$  is the RVE volume. The corresponding effective stiffness tensor  $\bar{C}$ , piezoelectric tensor  $\bar{e}$ , dielectric permittivity tensor  $\bar{\kappa}$ , thermal stress tensor  $\bar{\lambda}$  and pyroelectric  $\bar{p}$  are:

$$\begin{aligned} \bar{C}_{ijmn} &= \left\langle C_{ijmn}^* + C_{ijkl}^* M U_{k,l}^{mn} + e_{ijl}^* N U_{l,m}^{mn} \right\rangle \\ \bar{e}_{ijn} &= \left\langle e_{ijn}^* + C_{ijkl}^* M \Phi_{k,l}^n + e_{ijl}^* N \Phi_{l,m}^n \right\rangle \\ \bar{\kappa}_{in} &= \left\langle \kappa_{in}^* - e_{ikl}^* M \Phi_{k,l}^n + \kappa_{il}^* N \Phi_{l,m}^n \right\rangle \\ \bar{\lambda}_{ij} &= \left\langle \lambda_{ij}^* - C_{ijkl}^* M \Theta_{k,l} - e_{ijl}^* N \Theta_{l,m} \right\rangle \\ \bar{p}_i &= \left\langle p_i^* - e_{ikl}^* M \Theta_{k,l} - \kappa_{il}^* N \Theta_{l,m} \right\rangle \end{aligned} \quad (29)$$

Using expression provided in Eq. (11), the effective properties can be rewritten as

$$\bar{\mathbf{E}} = \langle \mathbf{E} + \mathbf{EM} \rangle, \quad \bar{\boldsymbol{\Pi}} = \langle \boldsymbol{\Pi} - \mathbf{EN} \rangle \quad (30)$$

where  $\mathbf{M} = [\mathbf{Mu}, \mathbf{M}\Phi; \mathbf{Nu}, \mathbf{N}\Phi]$  and  $\mathbf{N} = [\mathbf{M}\theta; \mathbf{N}\theta]$  with  $M_{uklm} = MU_{k,l}^{mn}$ ,  $M_{\phi kln} = M\Phi_{k,l}^n$ ,  $N_{mnl} = NU_{l,m}^{mn}$ ,  $N_{\phi ln} = N\Phi_{l,m}^n$ ,  $M_{\theta kl} = M\Theta_{k,l}$  and  $N_{\theta l} = N\Theta_{l,m}$ . It can be found from Eq. (30) that the effective properties for both coupled thermo-electro-mechanical fields and single

mechanical field share similar expressions based on AH method [58].

## 5. Numerical results and discussions

In this section, AH method developed in Section 4 is verified and implemented to study the effects of pore shape on four types of

thermo-piezoelectric materials (Type I, II, III and IV). More specifically, 2062 different pores (1482 for type I and II and 580 for type III and IV) are analyzed and their properties are compared to commonly used regular honeycomb piezoelectric cellular materials [34–36] and piezocomposites with embedded cylindrical inclusions [19–23].

### 5.1. Verification

Before conducting the following numerical analysis, the accuracy of the written code is firstly verified. The calculated results are compared with those results provided in previous references [59,60]. In Ref. [59], a 2D piezocomposite with inclusion in square shape is considered and AH has been used to predict the effective thermo-electro-mechanical properties. A 3D 1–3 piezocomposites structure has been also analyzed in Ref. [60], where SM homogenization was adopted to obtain the results. Table 1 lists the numerical results; it can be seen that there is no difference between our results and those presented in Ref. [59]; maximum difference between our numerical results and those given in Ref. [60] is 0.6%.

**Table 1**  
Comparison between the results obtained with the present code, Ref. [59] and Ref. [60].  $C$  in  $(\times 10^{10})$  Pa,  $e$  in  $(\times 10^{-2})$  C/m<sup>2</sup>,  $\kappa$  in  $(\times 10^{-11})$  C/(Vm<sup>2</sup>),  $\lambda$  in  $(\times 10^5)$  N/(mK),  $\gamma$  in  $(\times 10^{-5})$  K<sup>-1</sup>,  $p$  in  $(\times 10^{-7})$  C/(m<sup>2</sup>K). The error is in percent and  $f_v$  is the volume fraction of the matrix.

$f_v$	Effective Parameters	AH [59]	Present result	Error	$f_v$	Effective Parameters	SM [60]	Present result	Error
0.75	$C_{11}$	2.56	2.56	0	0.1	$C_{11}$	0.942	0.942	0
	$C_{12}$	2.56	2.56	0		$e_{33}$	0.166	0.167	0.6
	$C_{22}$	2.50	2.50	0		$\alpha_{33}$	5.17	5.16	0.2
	$C_{33}$	0.81	0.81	0	0.2	$C_{11}$	1.14	1.14	0
	$e_{11}$	0.0146	0.0146	0		$e_{33}$	0.475	0.476	0.2
	$e_{23}$	0.0076	0.0076	0		$\gamma_{33}$	4.40	4.41	0.2
	$\kappa_{11}$	7.19	7.19	0	0.3	$C_{11}$	1.41	1.41	0
	$\kappa_{22}$	7.20	7.20	0		$e_{33}$	1.09	1.09	0
	$\lambda_{11}$	4.49	4.49	0		$\gamma_{33}$	3.69	3.69	0
	$\lambda_{22}$	5.58	5.58	0	0.4	$C_{11}$	1.83	1.83	0
	$p_1$	8.88	8.88	0		$e_{33}$	2.57	2.58	0.4
	$p_2$	5.94	5.94	0		$\gamma_{33}$	2.99	2.99	0

**Table 2**

Piezoelectric properties of material constituents of piezoelectric cellular metamaterials:  $\mathbf{C}$  in ( $\times 10^{10}$ ) Pa,  $\mathbf{e}$  in ( $\times 10^{-2}$ ) C/m<sup>2</sup>,  $\kappa$  in ( $\times 10^{-11}$ ) C/(Vm<sup>2</sup>) [60].

Material	$C_{11}$	$C_{11}$	$C_{11}$	$C_{11}$	$C_{11}$	$e_{31}$	$e_{31}$	$e_{31}$	$\kappa_{11}$	$\kappa_{33}$
Epoxy	8	4.4	4.4	8	1.8	0	0	0	3.7	3.7
BaTiO <sub>3</sub>	150	66	66	146	4.4	-4.3	17.5	11.4	987.2	111.6

**Table 3**

Thermal properties of material constituent of piezoelectric cellular metamaterials  $\rho$  in g/cm<sup>3</sup>,  $\Delta$  in ( $\times 10^{-6}$  K<sup>-1</sup>) Pa,  $\gamma$  in Vm<sup>-1</sup>K<sup>-1</sup>,  $\mathbf{K}$  in Wm<sup>-1</sup>K<sup>-1</sup>,  $C_p$  in J/(gK) [60,61].

Material	$\rho$	$\Delta_{11}$	$\Delta_{33}$	$\gamma_3$	$K$	$C_p$
Epoxy	1.15	60	60	0	0.7	1.10
BaTiO <sub>3</sub>	5.70	8.53	1.99	13300	2.9	0.43

In the following subsections, an eco-friendly, biocompatible, and 3D printable material, BaTiO<sub>3</sub>, which shows both piezoelectric and pyroelectric properties has been selected as piezoelectric material. A non-piezoelectric epoxy has been used as the matrix for type III and IV cellular piezoelectric metamaterials. The piezoelectric properties of the constituent materials are given in Table 2 and their associated thermal properties are given in Table 3 [60,61].

## 5.2. Porous thermo-piezoelectric metamaterials made of a single material

A comprehensive study on type I and type II piezoelectric cellular metamaterials is presented here, which includes an investigation on the influence of shape parameters and polarization direction on effective properties and the relationship between effective properties and solid volume fraction.

### 5.2.1. Influence of shape parameters and polarization direction on effective piezoelectric properties for type I and type II metamaterials

To examine the effects of shape parameters, e.g.  $\alpha$ ,  $\beta$  and  $s$ , and polarization direction on effective piezoelectric properties of type I and type II metamaterials, Fig. 5 presents the variation of seven piezoelectric constants and four piezoelectric figures of merit for several selected pore shapes. More specifically,  $f_V$  and  $c_2$  are set as 0.7 and -0.2, respectively, while  $c_1$  varies as -0.4, -0.2, 0, 0.2 and 0.4 and  $s$  is selected as 0.5 and 1. Two groups of  $\alpha$  and  $\beta$  are considered, i.e.  $\alpha = 4$ ,  $\beta = 8$  and  $\alpha = 3$ ,  $\beta = 6$ . These selected shapes are sensitive to  $c_1$ ,  $c_2$  and  $s$  and most of them are admissible geometries. Compared to type I metamaterials, type II metamaterials are more sensitive to shape parameters and its piezoelectric figures of merit has also been improved. The following findings are made:

- (i) With the exception of  $k_t$  (Fig. 5 (j)), other piezoelectric properties of type I metamaterials are insensitive to pore shapes and share the same value with type I honeycomb.
- (ii) Type II metamaterials exhibit pronounced sensitivity to pore shapes. For example, by changing  $c_1$ ,  $\alpha$ ,  $\beta$  and  $s$ ,  $E_{33}$  changes from 32.99 GPa to 64.21 GPa and  $Z$  varies between 13.69 Mrayls and 19.12 Mrayls providing more flexibility for piezoelectric property selections. In addition, five fundamental piezoelectric properties along polarization direction, i.e.  $E_{33}$ ,  $e_{33}$ ,  $d_{33}$ ,  $\kappa_{33}$  and  $\kappa_{33}^\sigma$ , share similar pattern, which means the same influence of pore shapes on these properties.
- (iii) Original pore shapes (A category:  $\omega_r = 0$  and  $s = 1$ ), rotated pore shapes (C category:  $\omega_r = 45^\circ$  and  $s = 1$ ) and

scaled-rotated pore shapes (D category:  $\omega_r = 45^\circ$ ,  $s = 0.5$ ) have similar influence on type II metamaterials. For example,  $E_{33}$  varies between 41.15 GPa and 47.29 GPa, 41.15 GPa and 46.75 GPa, 32.99 GPa and 37.64 GPa for A, C, and D categories, respectively, while varies between 61.96 GPa and 64.20 GPa for B category. Furthermore, apart from  $d_{31}$ ,  $d_{32}$ ,  $d_h$  and  $d_h \times g_h$ , other seven piezoelectric properties of type II metamaterials for C category pore shapes are higher than those with A, C and D categories. For example, for type II metamaterials with  $\alpha = 3$ ,  $\beta = 6$ ,  $c_1 = 0$ ,  $\omega_r = 0$  and  $s = 0.5$ ,  $E_{33}$ ,  $e_{33}$ ,  $d_{33}$ ,  $\kappa_{33}$  and  $\kappa_{33}^\sigma$  are 64.25 GPa, 11.55 C/m<sup>2</sup>,  $0.19 \times 10^{-12}$  m/V,  $7.08 \times 10^{-9}$  C<sup>2</sup>/N/m<sup>2</sup> and 9.37 C<sup>2</sup>/N/m<sup>2</sup>, respectively, which are 37.96%, 35.09%, 3.0%, 14% and 19.66% higher than that of type II honeycombs. It should be mentioned  $\alpha$  and  $\beta$  have negligible influence on type II metamaterials.

- (iv) With transverse polarization, type II metamaterials have significant improvement on  $d_h$  and  $d_h \times g_h$ . Since  $d_{33}$  is positive, while  $d_{31}$  and  $d_{32}$  are negative, the reason for the improvement of  $d_h$  is transverse polarization decreases the absolute value of  $d_{31}$  and  $d_{32}$ . For example, for type II metamaterials with  $\alpha = 4$ ,  $\beta = 8$ ,  $c_1 = 0$ ,  $\omega_r = 0$  and  $s = 1$ ,  $d_{31}$ ,  $d_{32}$  and  $d_h$  are 34.31%, 60.96% and 195.28% higher than that of type I honeycombs, which is suitable for hydrophone devices. In addition, the decrease of  $\kappa_{33}^\sigma$  for type II metamaterials further improve  $d_h \times g_h$ . Since  $\kappa_{33}$  and  $\kappa_{33}^\sigma$  share the same variation trend and  $\kappa^\sigma = \kappa + e^T C^{-1} e$ , the variation of  $\kappa_{33}^\sigma$  only depends on  $\kappa_{33}$  and accordingly  $\kappa_{33}$  is only analyzed in the following analysis. However, with longitudinal polarization, type I metamaterials show a higher  $k_t$  and  $Z$ .

### 5.2.2. Influence of shape parameters and polarization direction on effective thermal and pyroelectric properties of type I and type II metamaterials

Fig. 6 illustrates the influence of pore shape parameters on the effective thermal and pyroelectric properties of type I and type II metamaterials. Overall, with the exception of  $\Delta_{33}$  and  $K_{33}$ , all other four properties are sensitive to pore shapes. In addition, type I and type II metamaterials share the same  $\Delta_{33}$  even with different shape parameters. Detailed observations are made as follows:

- (i) No matter how the pore shape changes for type I and type II cellular piezoelectric metamaterials, thermal expansion coefficient,  $\Delta_{33}$  (Fig. 6 (a)), always remains the same value as that of BaTiO<sub>3</sub>. This phenomenon, which has been mathematically proved in Appendix C by proposed asymptotic homogenization method, also holds for  $\Delta_{11}$ ,  $\Delta_{22}$  and  $\gamma_3$ . Therefore, it is impossible to tailor the thermal expansion of single material only by tailoring its microarchitecture.
- (ii) In Fig. 6(b)–6(e), different with piezoelectric properties,  $p_3$ ,  $F_l$ ,  $F_V$  and  $F'_E$  of type I metamaterial show obvious dependence on pore shapes. More specifically,  $p_3$  and  $F_l$  share the exact same pattern due to a constant solid volume fraction and heat capacity (see Eq. (11)). Similar to fundamental piezoelectric properties along direction 3 of type II metamaterials (e.g., Fig. 5(b)),  $p_3$  and  $F_l$  are smaller than that of type I metamaterials and scaling the pore shapes of type II metamaterials decreases this difference. The same trend also occurs for  $F'_E$  (see Fig. 6(e)). However, in Fig. 6(d), due to the decrease of  $\kappa_{33}^\sigma$  of type II metamaterials,  $F_V$  of type II metamaterial is higher than that of type I metamaterials. In addition,  $F_V$  of type II honeycomb is smaller than that of type

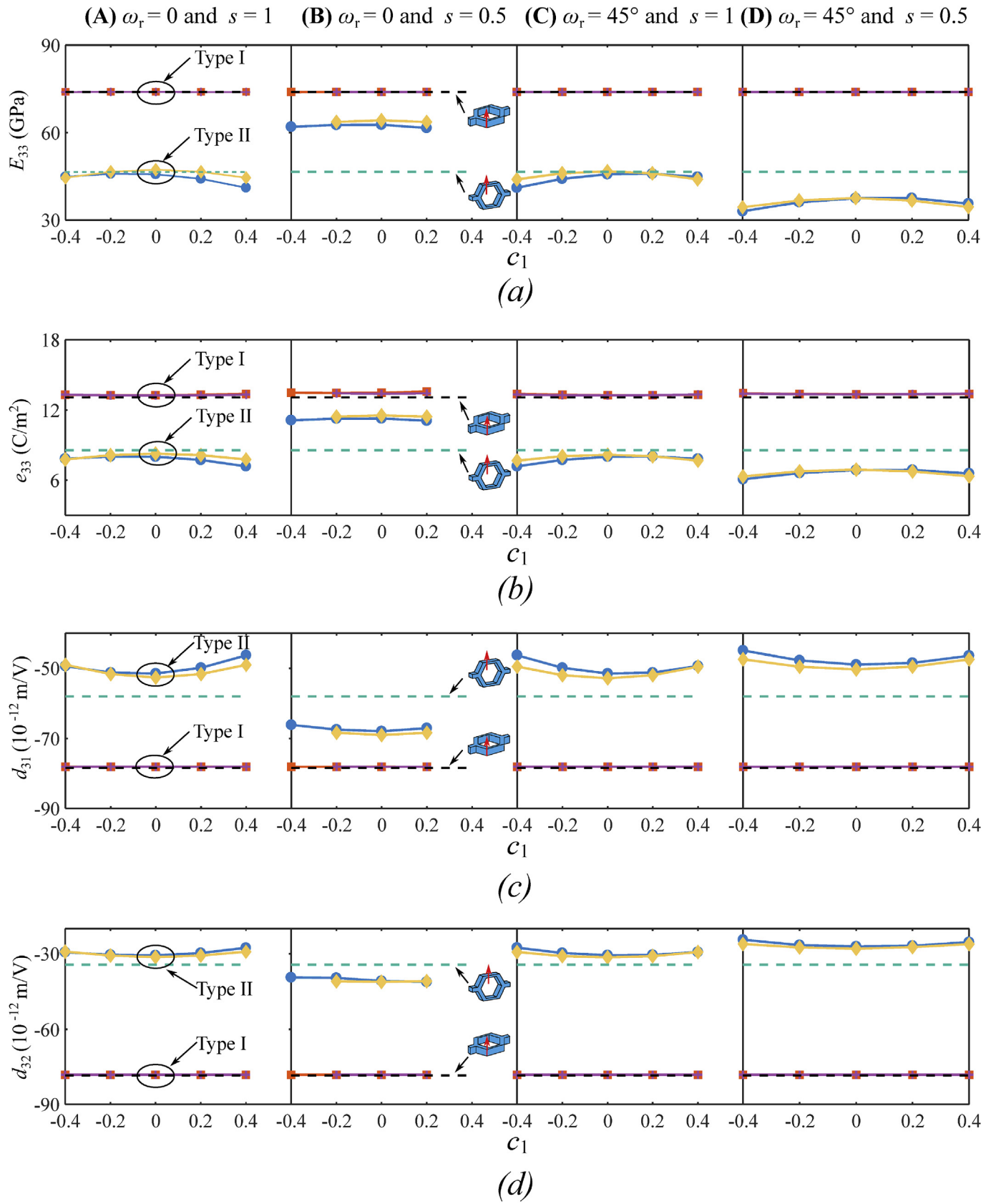


**Fig. 5.** Variation of piezoelectric properties and figures of merit of type I and type II cellular metamatteials with solid volume fraction  $f_v = 0.7$  and shape coefficient  $c_2 = -0.2$ .

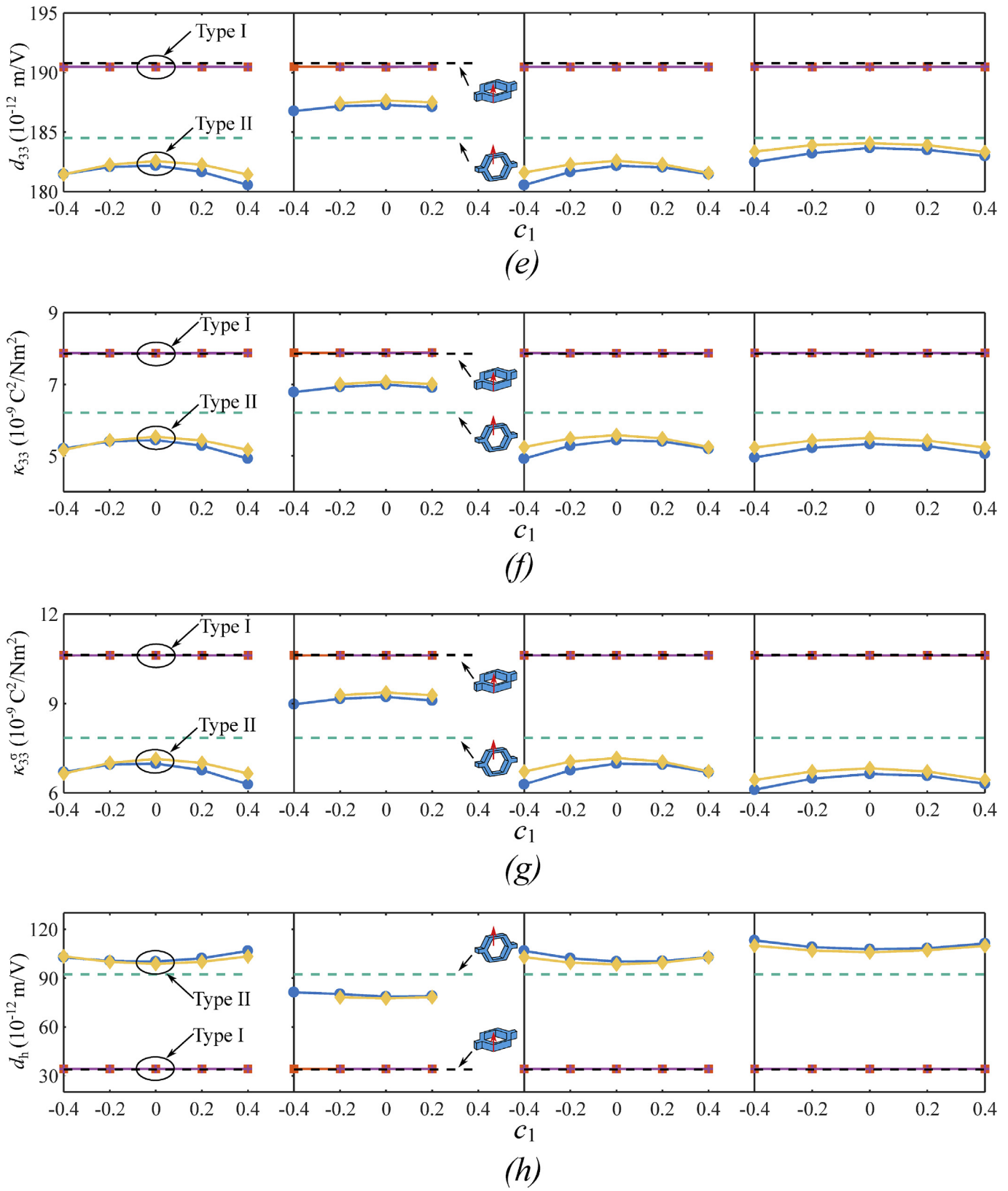


Fig. 5. (continued).

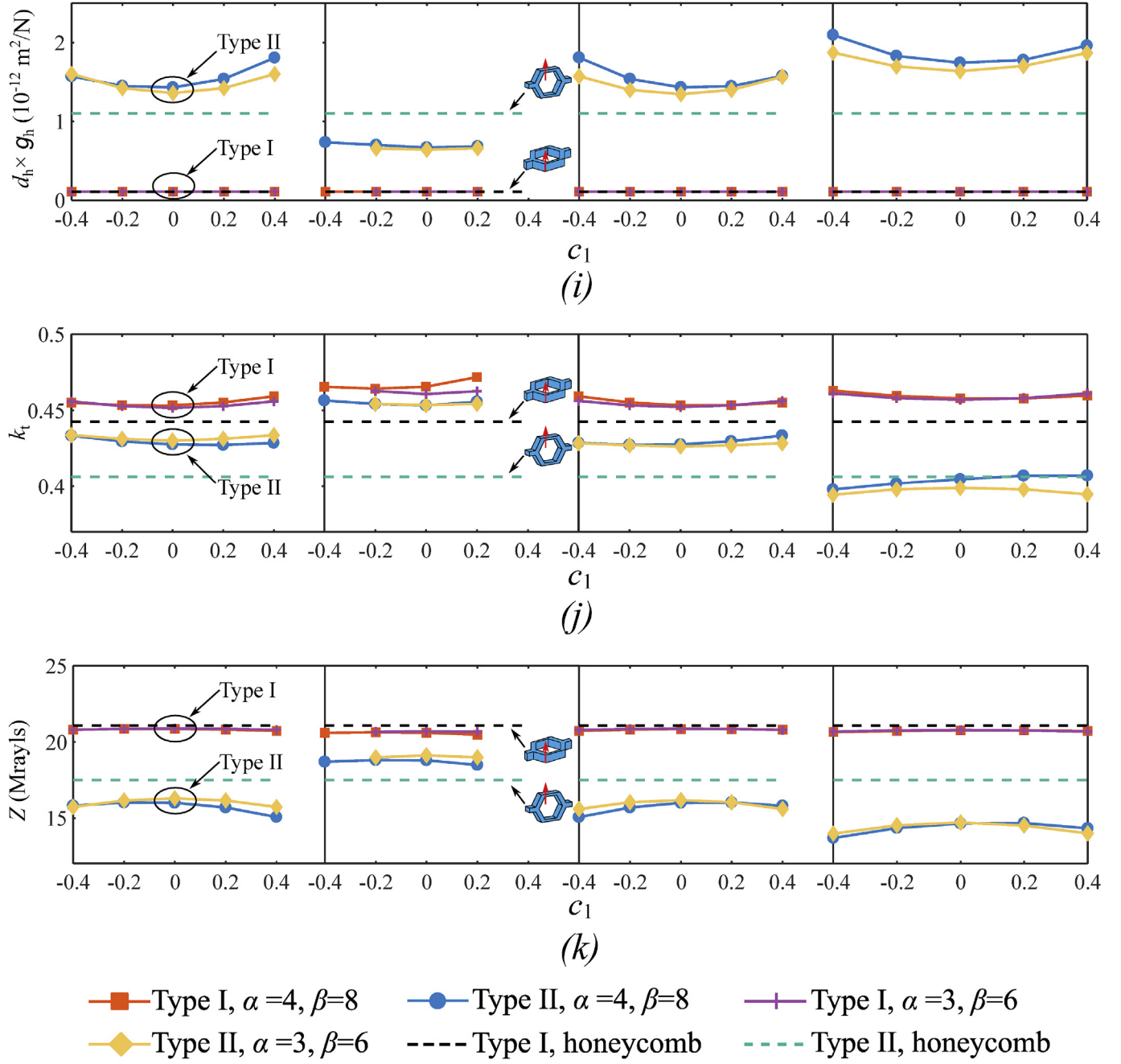


Fig. 5. (continued).

I honeycombs, indicating that the decrease of  $\kappa_{33}^g$  of type II metamaterials cannot compensate the smaller value of  $p_3$  based on Eq. (11).

- (iii) In Fig. 6(f),  $K_{33}$  of type I metamaterials is insensitive to pore shapes and are higher than that of type II metamaterials. In addition, scaling the pore shape (B category) will also increase this value for type II metamaterials.

### 5.2.3. Relation between effective thermo-electro-mechanical properties and solid volume fraction

In order to understand the relationship between thermo-electro-mechanical properties and volume fraction of solid phase or porosity, Fig. 7 presents seven piezoelectric related properties

and five thermal related properties for type I (light red area) and type II metamaterials (light blue area) with  $f_v$  varying from 0.3 to 1. For considered metamaterials,  $c_1$  and  $c_2$  are selected as  $-0.4, -0.2, 0, 0.2$  or  $0.4$ , while two groups of  $\alpha$  and  $\beta$ , i.e.  $\alpha = 4, \beta = 8$  and  $\alpha = 3, \beta = 6$ , are chosen for generating the microarchitectures. The pore shapes are tailored by rotating and scaling the pores for the following four sets:  $\omega_r = 0$  and  $s = 1$  (original shape),  $\omega_r = 0$  and  $s = 0.5$  (scaled pore),  $\omega_r = 45^\circ$ ,  $s = 1$  (rotated pore) and  $\omega_r = 45^\circ$  and  $s = 0.5$  (rotated and scaled pore). Omitting inadmissible pore architectures, 1482 different cellular piezoelectric metamaterials are analyzed.

As expected, apart from  $k_t$  (Fig. 7(g)),  $p_3$  (Fig. 7(i)) and three pyroelectric figures of merit ((Fig. 7(j) – (l))), all other properties of type I metamaterials is linear with solid volume fraction, which is

(A)  $\omega_r = 0$  and  $s = 1$  (B)  $\omega_r = 0$  and  $s = 0.5$  (C)  $\omega_r = 45^\circ$  and  $s = 1$  (D)  $\omega_r = 45^\circ$  and  $s = 0.5$

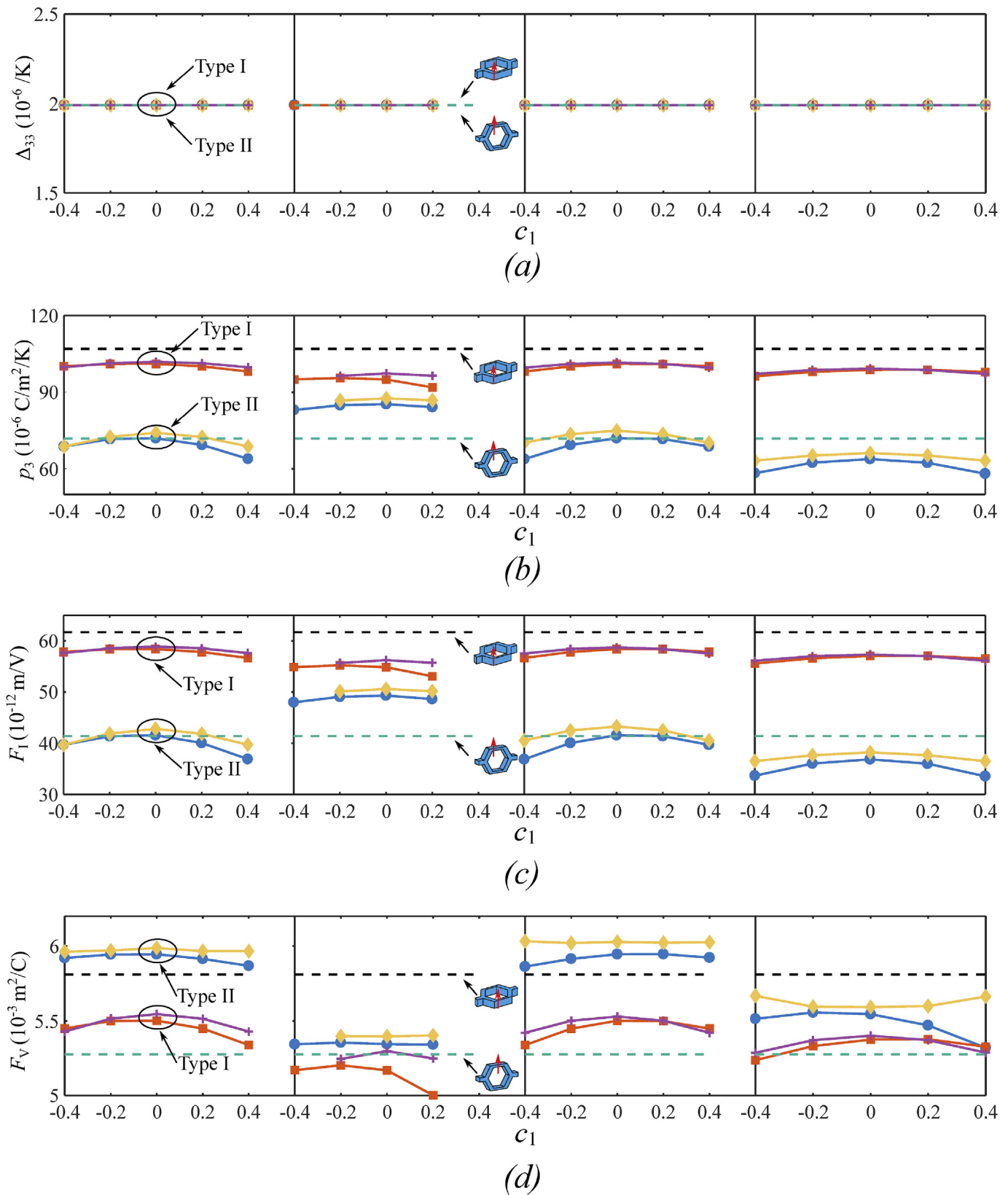


**Fig. 6.** Variation of the thermal-related properties and associated figure of merits of type I and type II cellular metamaterials with a solid volume fraction  $f_v = 0.7$  and shape coefficient  $c_2 = -0.2$ .

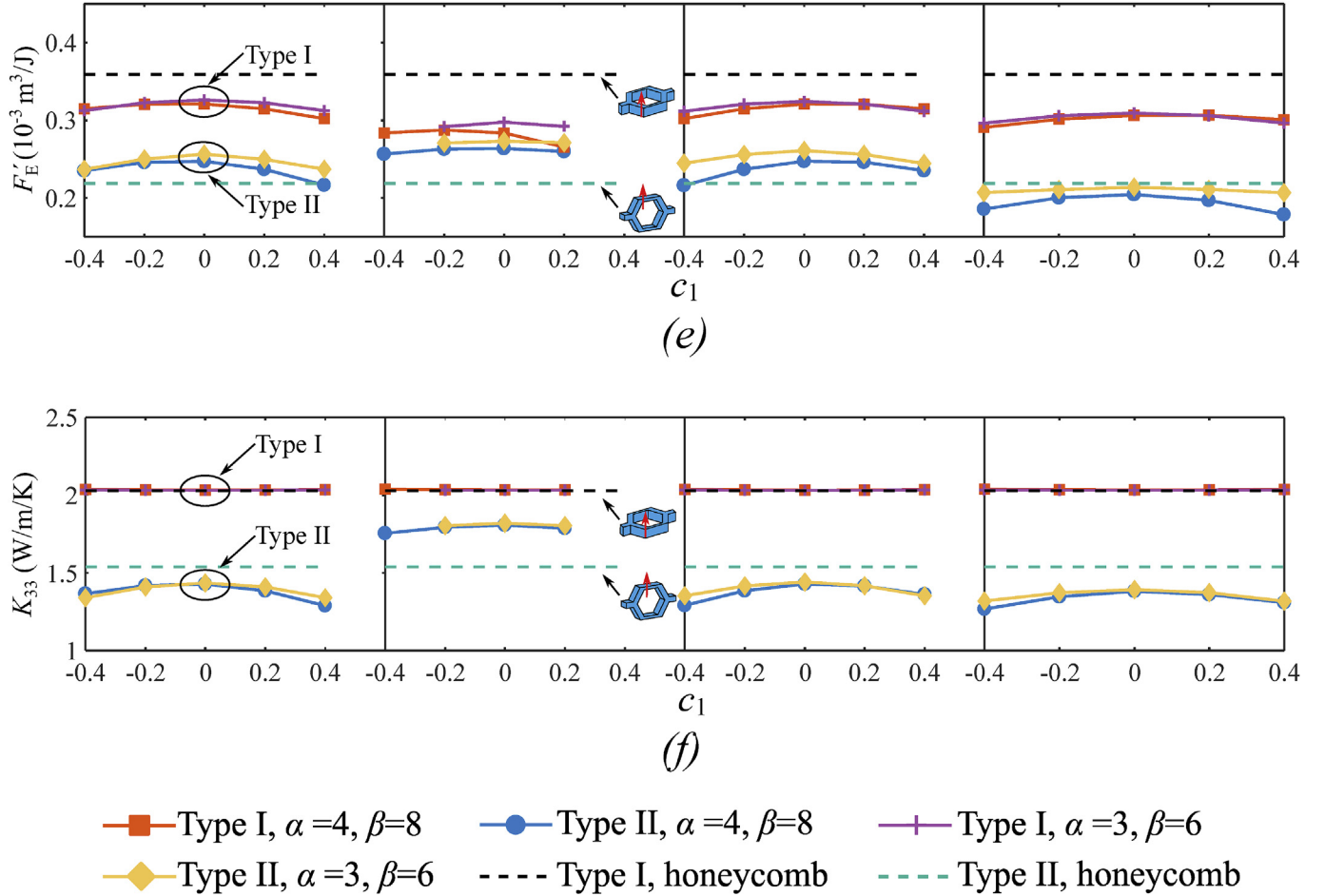


Fig. 6. (continued).

due to their insensitivity to pore shapes. In the meantime, type II metamaterials offer a wider range of material property selections for design. More specifically:

- (i) As found in Figs. 5 and 6, fundamental piezoelectric properties and thermal conductivity along 3 direction, i.e.  $E_{33}$ ,  $e_{33}$ ,  $\kappa_{33}$  and  $K_{33}$ , share similar variation trend with respect to shape parameters. Therefore, as shown in Fig. 7(a) – (d),  $E_{33}$ ,  $e_{33}$ ,  $\kappa_{33}$  and  $K_{33}$  for both type I and type II metamaterials have same property pattern, where type I metamaterials have higher values while type II metamaterials provide more property selections.
- (ii) As discussed in Section 5.2.1, type II metamaterials have much better performance on  $d_h$  and  $d_h \times g_h$ . In addition, in Fig. 7(e) and (f),  $d_h$  and  $d_h \times g_h$  increase by decreasing the volume fraction and tailoring pore shapes is an effective method to further improve these two values. For example, for type II metamaterials with  $f_v = 0.6$ , the maximum and minimum  $d_h$  values are  $142.39 \times 10^{-12} \text{ m/V}$  and  $83.36 \times 10^{-12} \text{ m/V}$ , which are 320% and 146% higher than type I honeycombs with  $f_v = 0.6$ .
- (iii) Except type II honeycomb (green dashed line), piezoelectric coupling constant,  $k_t$ , of type I and type II cellular metamaterials with a circular pore and type I honeycomb show a decreasing trend by increasing the volume fraction. In contrast to  $d_h$  and  $d_h \times g_h$ , type I metamaterials always show a maximum  $k_t$  value. For acoustic transducer applications, such as hydrophone, lower values of  $Z$  are desired for better

performance. Therefore, the decrease of  $Z$  value by increasing porosity indicates that cellular piezoelectric metamaterials can improve the acoustic impedance of piezoelectric materials.

- (iv) Similar to Fig. 6(b) and (c), it can be found that  $p_3$  (Fig. 7(i)) and  $F_l$  (Fig. 7(j)) share the same property patterns (Eq. (11)). In addition, increasing volume fraction will generally improve  $p_3$  and  $F_l$  and type I metamaterials always have higher  $p_3$  and  $F_l$  than type II metamaterials. Therefore, introducing porosity and transverse polarization is not appropriate for improving pyroelectric coefficient and current responsivity.
- (v) Opposed to  $p_3$  and  $F_l$ ,  $F_V$  (Fig. 7(k)) has a decreasing trend by increasing solid volume fraction and type II metamaterials generally provide a higher value for  $F_V$ . Therefore, the combination of increasing porosity and tailoring pore shapes of type II metamaterials can enhance voltage responsivity. Decreasing volume fraction can improve  $F_E$  (Fig. 7(l)) of type I metamaterial but not for type II metamaterials. Furthermore, type I metamaterials show higher  $F_E$  than type II metamaterials. Therefore, compared to type II metamaterials, type I porous metamaterials are suitable material selections for pyroelectric energy harvesting application.

#### 5.2.4. Comparison between type I and type II metamaterials and conventional honeycomb piezoelectric material

In order to provide quantitative comparison between

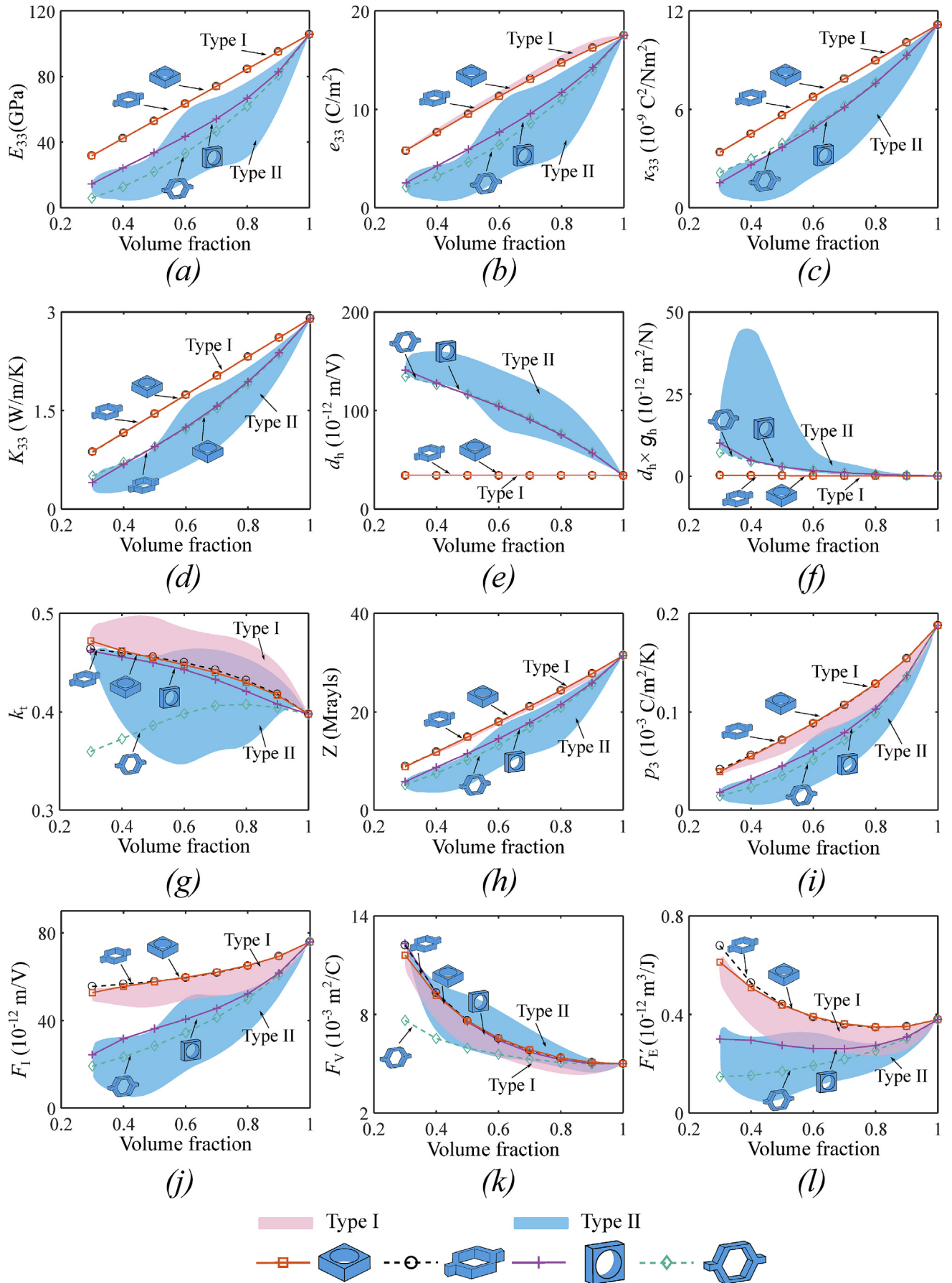
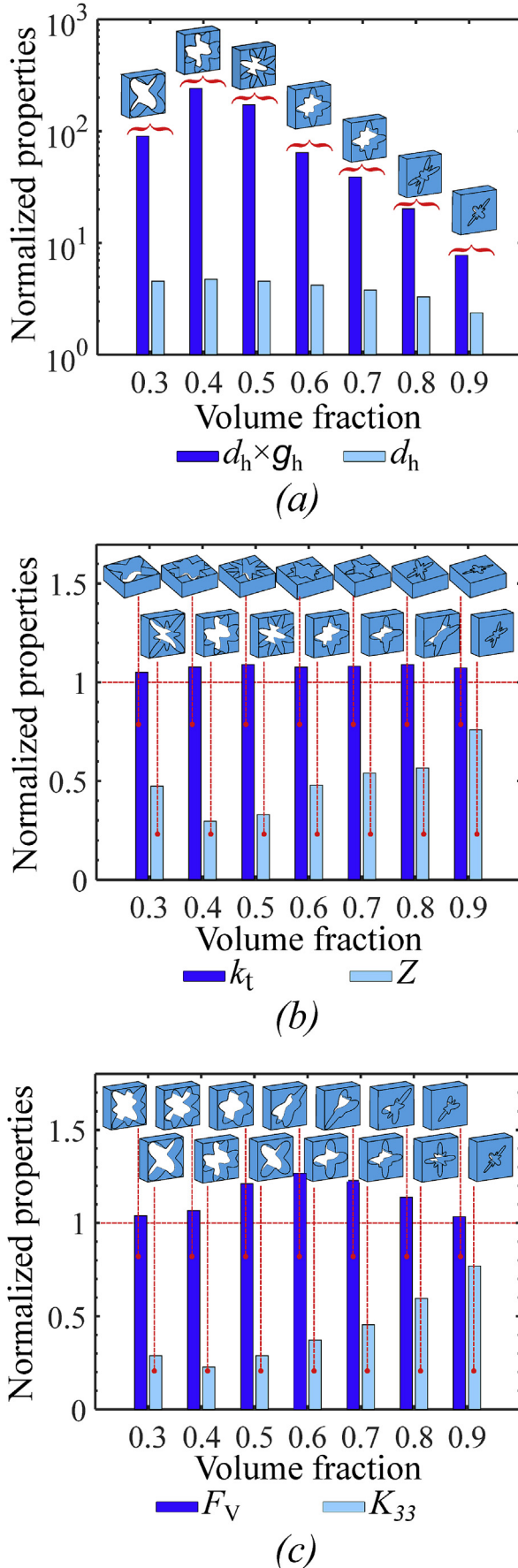


**Fig. 7.** Property and figures of merit design charts for type I and type II cellular piezoelectric metamaterials with solid volume fracture  $f_v$  varying from 0.3 to 1.



architected cellular piezoelectric metamaterials and conventional honeycomb piezoelectric materials, Fig. 8 presents normalized optimum figures of merit shown in Fig. 7, where maximum values of  $d_h$ ,  $d_h \times g_h$ ,  $k_t$ ,  $F_V$ , and minimum values of  $Z$  and  $K_{33}$  at different volume fractions are normalized by type I honeycomb piezoelectric materials with the same solid volume fraction.  $F_I$  and  $F'_E$  of cellular piezoelectric metamaterials are not presented here since their optimum values belong to honeycomb piezoelectric materials (Fig. 7(j) and (l)). As shown in Fig. 8(a), the microarchitectures with optimum  $d_h$  and  $d_h \times g_h$  vary for different volume fractions. The improvement, however, decreases when the volume fraction increases. For example, when  $f_v$  is 0.4,  $d_h$  is increased by 375%, while the increase is 138% for  $f_v = 0.9$ . The achievable improvement for  $k_t$  is not considerable as shown in Fig. 8(b); the optimum normalized values of  $k_t$  only changes in the range from 4.8% to 7.4% for different values of volume fraction, all belong to type I metamaterials. However, type II metamaterials show the optimum normalized values for  $Z$ ;  $Z$  can be decreased by 70.44% compared to a honeycomb piezoelectric counterpart when  $f_v = 0.4$ . It is worth mentioning that lower  $Z$  means better performance for underwater acoustic transducers. In Fig. 8(c), it can be seen that there is modest improvement for  $F_V$  (IR detection), increased by 3.4% ~ 26.5%, and significant decrease for  $K_{33}$  by 23.18% ~ 77.24%, which is appropriate for thermal insulation applications.

### 5.3. Porous thermo-piezoelectric metamaterials with bi-phase materials

Another two types of metamaterials, type III and type IV, are discussed in this section. Apart from pore shapes and polarization direction, the influence of pore and inclusion volume fraction on the effective properties is also considered.

#### 5.3.1. Influence of inclusion and pore volume fraction on effective piezoelectric properties of type III and type IV metamaterials

Fig. 9 shows the relationship between nine piezoelectric properties and inclusion volume fraction,  $f_{vi}$ . Here, two pore volume fractions,  $f_{pore} = 0.1$  and  $f_{pore} = 0.3$  and two pore shapes with  $\alpha = 4$ ,  $\beta = 8$ ,  $c_1 = 0$ ,  $c_2 = 0$  (blue line) and  $\alpha = 4$ ,  $\beta = 8$ ,  $c_1 = -0.4$ ,  $c_2 = 0$  (red line), are considered. Due to the inadmissible geometry, inclusion volume fraction varies from 0.3 to 0.6 for  $f_{pore} = 0.1$ , while it changes between 0.2 and 0.4 for  $f_{pore} = 0.3$ . In general, both inclusion and pore volume fraction are important factors for determining effective piezoelectric properties of type III and type IV metamaterials. However, apart from  $k_t$ , inclusion volume fraction has more obvious influence on these properties. In addition, effective piezoelectric properties are greatly affected by the polarization direction, while almost insensitive to pore shapes, except four piezoelectric figures of merit of type IV metamaterials. In specific:

- (i) The three fundamental piezoelectric properties along polarization direction, i.e.  $E_{33}$  (Fig. 9(a)),  $K_{33}$  (Fig. 9(b)) and  $K'_{33}$  (Fig. 9(c)) of type III metamaterials show linear relationship with inclusion volume fraction, while they show nonlinear relationship for type IV metamaterials. In addition,  $f_{pore}$  does not show significant influence on these three properties. For example, for type III metamaterials with  $c_1 = 0$  and  $c_2 = 0$ ,  $K_{33}$  is  $3.41 \times 10^{-9} \text{ C}^2/\text{Nm}^2$  when  $f_{pore} = 0.3$  and  $f_{vi} = 0.3$ , while the corresponding value for  $f_{pore} = 0.1$  and  $f_{vi} = 0.3$  is  $3.40 \times 10^{-9} \text{ C}^2/\text{Nm}^2$ . It should be mentioned that  $K_{33}$  and  $K'_{33}$  share the same trend for type III and type IV metamaterials. Therefore, in the following analysis,  $K_{33}$  is only discussed for type III and type IV metamaterials.

Fig. 8. Normalized maximum figures of merit of Type I and type II piezoelectric cellular metamaterials.

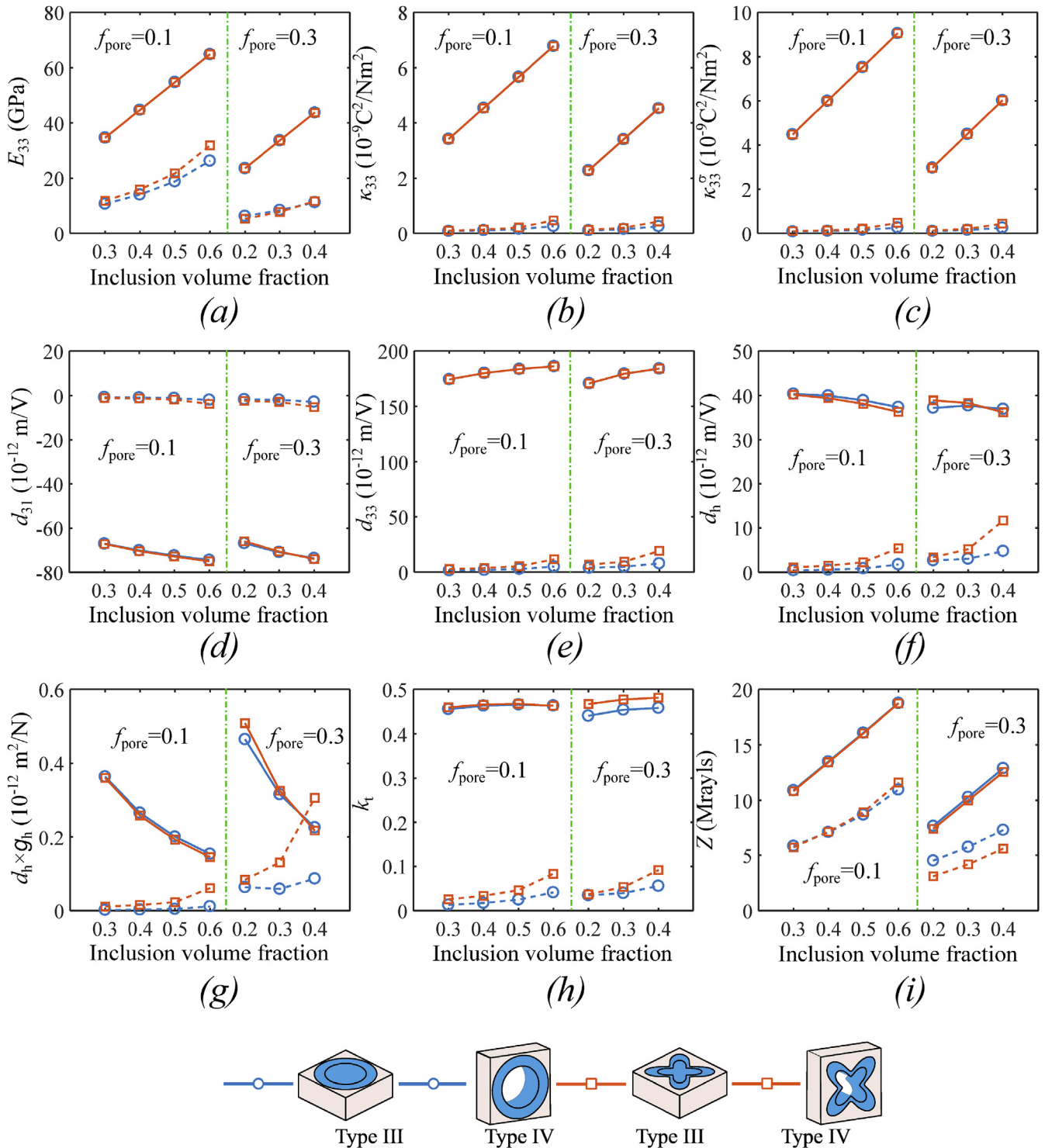


**Fig. 9.** Influence of inclusion and pore volume fraction on piezoelectric properties of type III and type IV cellular metamaterials with pore volume fractions  $f_{\text{pore}} = 0.1$  and  $0.3$ ,  $\alpha = 4$ ,  $\beta = 8$ ,  $c_1 = 0$  and  $c_2 = 0$  (blue line),  $c_1 = -0.4$  and  $c_2 = 0$  (red line). (For interpretation of the references to color in this figure legend, the reader is referred to the Web version of this article.)

- (ii) Although decreasing the inclusion volume fraction enhances both  $d_h$  (Fig. 9(g)) and  $d_h \times g_h$  (Fig. 9(g)) for type III metamaterials, it is not the same case for considered type IV metamaterials. In addition, for  $d_h$ , different polarization directions result in a considerable difference between type III and type IV metamaterials. However, it is the inclusion volume fraction that determines  $d_h \times g_h$  for both types of

metamaterials. The reason is that although transverse polarization can significantly increase  $d_{31}$  (dash lines in Fig. 9(d)) almost to a zero value, its  $d_{33}$  is also decreased to a small value; as a result, the value of  $d_h$  for type IV metamaterials is still smaller than that of type III metamaterials. However, with smaller  $\kappa_{33}^\sigma$ , type IV metamaterials can even show a higher  $d_h \times g_h$ . For example, when  $c_1 = -0.4$ ,  $c_2 = 0$ ,

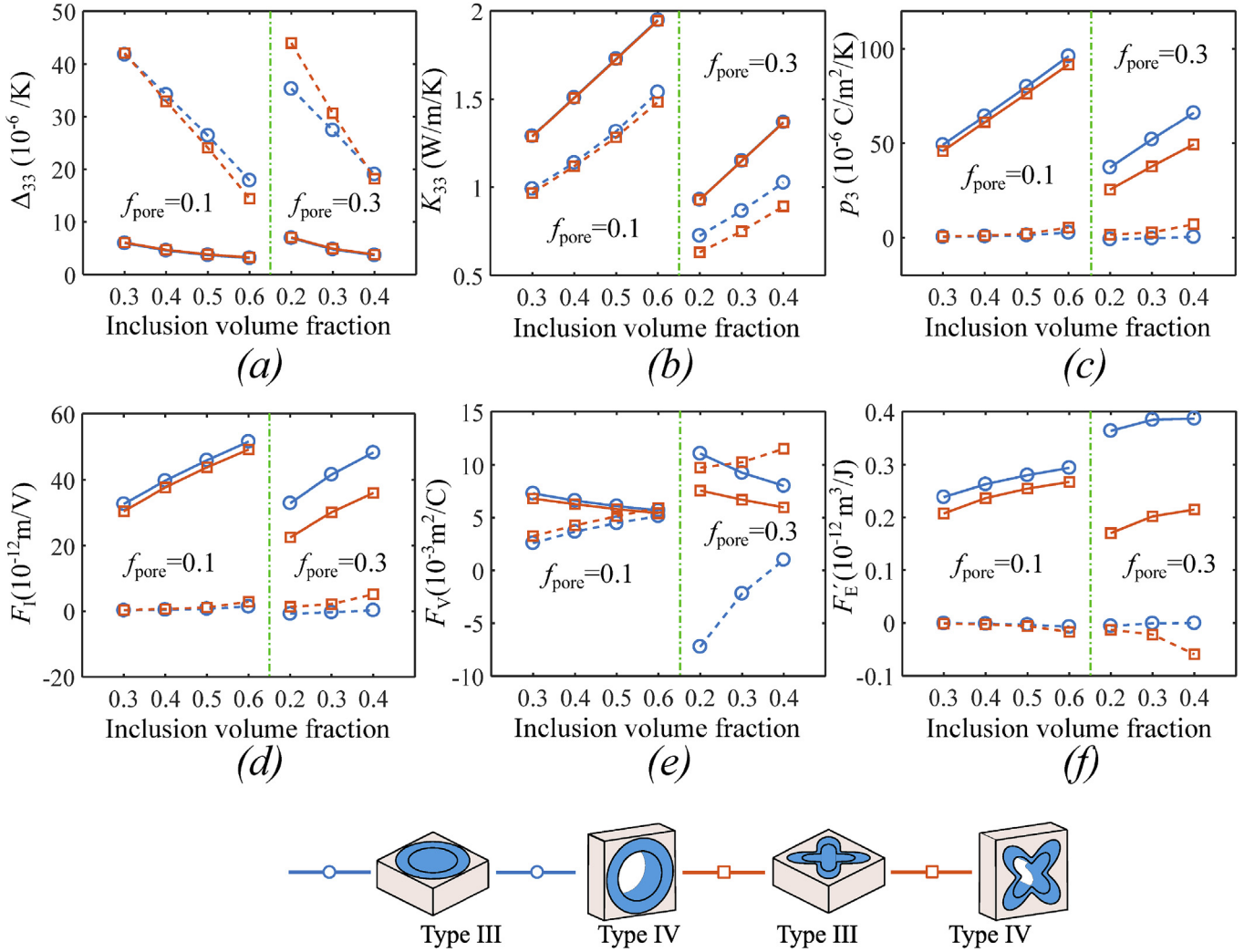


**Fig. 10.** Influence of inclusion and pore volume fraction on the thermal related properties of type III and type IV cellular metamaterials with pore volume fractions  $f_{\text{pore}} = 0.1$  and  $0.3$ ,  $\alpha = 4$ ,  $\beta = 8$ ,  $c_1 = 0$  and  $c_2 = 0$  (blue line),  $c_1 = -0.4$  and  $c_2 = 0$  (red line). (For interpretation of the references to color in this figure legend, the reader is referred to the Web version of this article.)

- $f_{\text{pore}} = 0.3$ ,  $f_{\text{vi}} = 0.4$ ,  $d_h$  for type IV metamaterials (i.e.  $3.06 \times 10^{-13} \text{ m}^2/\text{N}$ ) is 41% higher than that of type III metamaterials (i.e.,  $2.17 \times 10^{-13} \text{ m}^2/\text{N}$ ).
- (iii) Similar to  $d_h$ ,  $k_t$  for longitudinally polarized type III metamaterials shows obvious superiority over the type IV metamaterials. However, smaller inclusion volume fractions for both type III and type IV result in better acoustic impedance (smaller  $Z$ ).

### 5.3.2. Influence of inclusion and pore volume fraction on effective thermal and pyroelectric properties of type III and type IV metamaterials

Fig. 10 illustrates the variation of six thermal related properties with respect to different inclusion and pore volume fractions for type III and type IV metamaterials. Overall, all six values of both type III and type IV metamaterials show dependence on inclusion and pore volume fraction. In addition, apart from  $F_V$ , polarization direction plays an important role for determining the effective thermal and pyroelectric properties of type III and type IV metamaterials. More specifically:

- (i)  $\Delta_{33}$  (Fig. 10 (a)) for both types of metamaterials shows a decreasing trend by increasing inclusion volume fraction, where  $\Delta_{33}$  for type III metamaterials are always smaller than that of type IV metamaterials. However,  $K_{33}$  (Fig. 10 (b)) shows a different trend, where  $K_{33}$  of four considered metamaterials linearly increases by increasing their inclusion volume fraction.
- (ii) For transverse polarization,  $p_3$  (Fig. 10 (c)) of type III metamaterials are much higher than that of type IV metamaterials which linearly increases with inclusion volume fraction. In the meantime, increasing pore volume fraction also improves  $p_3$  of both types of metamaterials. It should be mentioned that since positive  $p_3$  of type IV metamaterials decreases to zero for small inclusion volume fraction, for some specific pore shapes, negative  $p_3$  can be found from type IV metamaterials, a similar behavior which has been reported previously for negative thermal expansion coefficient of bi-material lattices [62]. For example, for  $c_1 = -0$ ,  $c_2 = 0$ ,  $f_{\text{pore}} = 0.2$  and  $f_{\text{vi}} = 0.3$ ,  $p_3$  is negative and its value is:  $p_3 = -0.91 \times 10^{-6} \text{ C/m}^2/\text{K}$ .

- (iii) Pore shapes and inclusion and pore volume fraction are important factors in determining  $F_V$  for type III and type IV metamaterials. When  $f_{\text{pore}} = 0.1$ ,  $F_V$  can be slightly affected by pore shapes and inclusion volume fraction. However, when  $f_{\text{pore}} = 0.3$ , a proper selection of pore shapes and inclusion volume fraction can lead to a wider range for  $F_V$ .  $F'_E$  (Fig. 10(f)) is greatly affected by polarization direction, where type III metamaterials are more suitable for pyroelectric energy harvesting. In addition, for higher pore volume fractions, tailoring pore shapes is also an efficient method to improve  $F'_E$ .

### 5.3.3. Relation between effective thermo-electro-mechanical properties of type III and type IV metamaterials and inclusion volume fraction

Fig. 11 shows 12 piezoelectric and pyroelectric property areas for type III and type IV cellular piezoelectric metamaterials, where seven groups of ( $f_{\text{pore}}, f_{Vi}$ ) are selected for presentation: (0.1, 0.3), (0.1, 0.4), (0.1, 0.5), (0.1, 0.6), (0.3, 0.2), (0.3, 0.3) and (0.3, 0.4). The pore shapes considered in Fig. 11 are determined by the same shape parameters mentioned in Fig. 7. Therefore, there are 580 different admissible geometries for type III and type IV metamaterials. In addition, the commonly used type III (red solid line) and type IV (black dash line) metamaterials with solid circular inclusion ( $c_1 = c_2 = f_{\text{pore}} = 0$ ) are given in Fig. 11. Overall, type IV metamaterials are more sensitive to pore shapes and give more flexibility for material property selections. However, with longitudinal polarization, apart from  $d_h \times g_h$  (Fig. 11(d)),  $\Delta_{33}$  (Fig. 11(g)),  $F_V$  (Fig. 11(k)) and  $F'_E$  (Fig. 11(l)), type III metamaterials always have higher values for all other involved properties. More specifically:

- (i)  $E_{33}$  and  $\kappa_{33}$  of type III metamaterials are almost insensitive to pore shapes and increase linearly by increasing inclusion volume fraction. Although  $E_{33}$  of type IV metamaterials show independence on inclusion volume fraction,  $\kappa_{33}$  of type IV metamaterials are more affected by pore shapes.
- (ii) For type III metamaterials, changing inclusion and pore volume fraction can slightly improve  $d_h$  (Fig. 11(c)). However, type III metamaterials with solid circular inclusion always have the highest  $d_h$ . On the contrary, by tailoring pore shapes, type IV metamaterials can achieve higher  $d_h \times g_h$  (Fig. 11(d)), where large pore volume fractions (orange area) exhibit more potential for better hydrophone signal-to-noise performance.
- (iii) The value of  $k_t$  remains the same value for Type III metamaterials for different inclusion volume fractions (Fig. 11(e)). However, for both type III and type IV metamaterials,  $Z$  (Fig. 11(f)) shows obvious increase by increasing the inclusion volume fraction.
- (iv) By tailoring pore shapes, type IV metamaterials can provide a wider selection for thermal expansion coefficient  $\Delta_{33}$ . For example, based on different pore shapes and inclusion volume fractions, type IV metamaterials with  $f_{\text{pore}} = 0.3$  (orange area in Fig. 11(g)) provide  $\Delta_{33}$  variation in the range of  $21.2 \times 10^{-6} \text{ K}^{-1}$  and  $68.5 \times 10^{-6} \text{ K}^{-1}$ . In addition, type III metamaterials always give the smallest  $\Delta_{33}$ . For both type III and type IV metamaterials, increasing inclusion volume fraction will increase  $K_{33}$  (Fig. 11(h)) and tailoring pore shapes has negligible influence on  $K_{33}$ .
- (v) As expected,  $p_3$  (Fig. 11(i)) and  $F_l$  (Fig. 11(j)) share the same pattern and increasing inclusion volume fraction enhances pyroelectric effect and current responsivity of type III metamaterials. However, for  $F_V$  (Fig. 11(k)) and  $F'_E$  (Fig. 11(l)), tailoring the pore shapes is an effective method to obtain

higher values to improve the performance of cellular piezoelectric metamaterials for IR detection and pyroelectric energy harvesting. For example, compared to type III metamaterials with  $\alpha = 4$ ,  $\beta = 8$ ,  $c_1 = c_2 = f_{\text{pore}} = 0$  and  $f_{Vi} = 0.3$  (solid red line),  $F_V$  and  $F'_E$  can be improved by 269.5% and 129.4% (Type IV metamaterials with  $\alpha = 4$ ,  $\beta = 8$ ,  $\omega_r = 45^\circ$ ,  $s = 0.5$  and  $c_1 = c_2 = -0.2$ ), respectively.

### 5.4. Comparison between type I, II, III, and IV metamaterials

A quantitative comparison between type I, type II, type III and type IV cellular piezoelectric metamaterials are provided in Table 4, where all values are normalized by the corresponding values of type I honeycomb metamaterials. Both  $E_{33}$  and  $\kappa_{33}$  of type I and III metamaterials are higher than their counterparts of type II and type IV metamaterials.  $d_{31}$ ,  $d_{32}$  and  $d_{33}$  of type II, type III and type IV metamaterials are all smaller than the corresponding properties of type I metamaterials. However, due to the different signs of  $d_{31}$  and  $d_{32}$  with  $d_{33}$ , type II and type III metamaterials have better hydrophone performance, while type IV metamaterials almost have zero  $d_h$  and  $d_h \times g_h$ . The improvement for  $k_t$  is limited and the highest value is reported for type I metamaterials. Both type II and type IV metamaterials show smaller  $Z$  compared to type I and type III metamaterials. However, due to the poor performance of type IV metamaterials for  $d_h$ ,  $d_h \times g_h$  and  $k_t$ , type II metamaterials are more suitable for piezoelectric applications. For thermal related properties,  $\Delta_{33}$  can be greatly increased by type III and type IV metamaterials, while remains the same value for type I and type II metamaterials. Both longitudinal polarization and introducing matrix with higher  $K_{33}$  can be used to obtain higher effective thermal conductivity  $K_{33}$ . Therefore, type III metamaterials have the highest  $K_{33}$ , while type II metamaterials have the smallest one. Although type III metamaterials have the highest  $p_3$ , for pyroelectric figures of merit of  $F_l$ ,  $F_V$  and  $F'_E$ , type I metamaterials show better overall performance. It should be mentioned that since thermo-electro-mechanical properties of type IV metamaterials strongly depend on pore shapes, these properties for type IV metamaterials as presented in Table 4 can be tuned arbitrarily.

Fig. 12 shows lightweighting and multifunctional potentials of piezoelectric metamaterials considered in this paper. Here,  $\bar{\rho}$  is density of metamaterial and  $(\cdot)^s$  means the properties of solid BaTiO<sub>3</sub>. It is clear that type II metamaterials simultaneously possess the best hydrophone sensitivity and hydrophone signal-to-noise ratio (Fig. 12(a)). Type II metamaterials also hold this advantage for lightweight hydrophone design (Fig. 12(b)). As shown in Fig. 12(c), type I metamaterials have combination of large  $Z/Z^s$  and  $k_t/(k_t)^s$ , while type II metamaterials have combination of smallest  $Z/Z^s$  and reasonable  $k_t/(k_t)^s$ . However, for a given mass, type II metamaterials have potential to design lightweight materials with smallest acoustic impedance and highest energy coupling factor, similar as that of type I and type III metamaterials (Fig. 12(d)). For pyroelectric application, type I metamaterials, especially type I honeycomb, are the most suitable cellular piezoelectric metamaterials for designing lightweight devices with the best current responsivity and pyroelectric energy harvesting performance (Fig. 12(e) and (f)). However, in Fig. 12(g) and (h), type IV metamaterials provide the highest voltage responsivity, while type I metamaterials still show the highest value for pyroelectric energy harvesting figure of merit.

## 6. Discussion

The architected cellular piezoelectric metamaterials analyzed in this work represent four distinct classes of cellular solids in terms of polarization direction and number of material phases for different

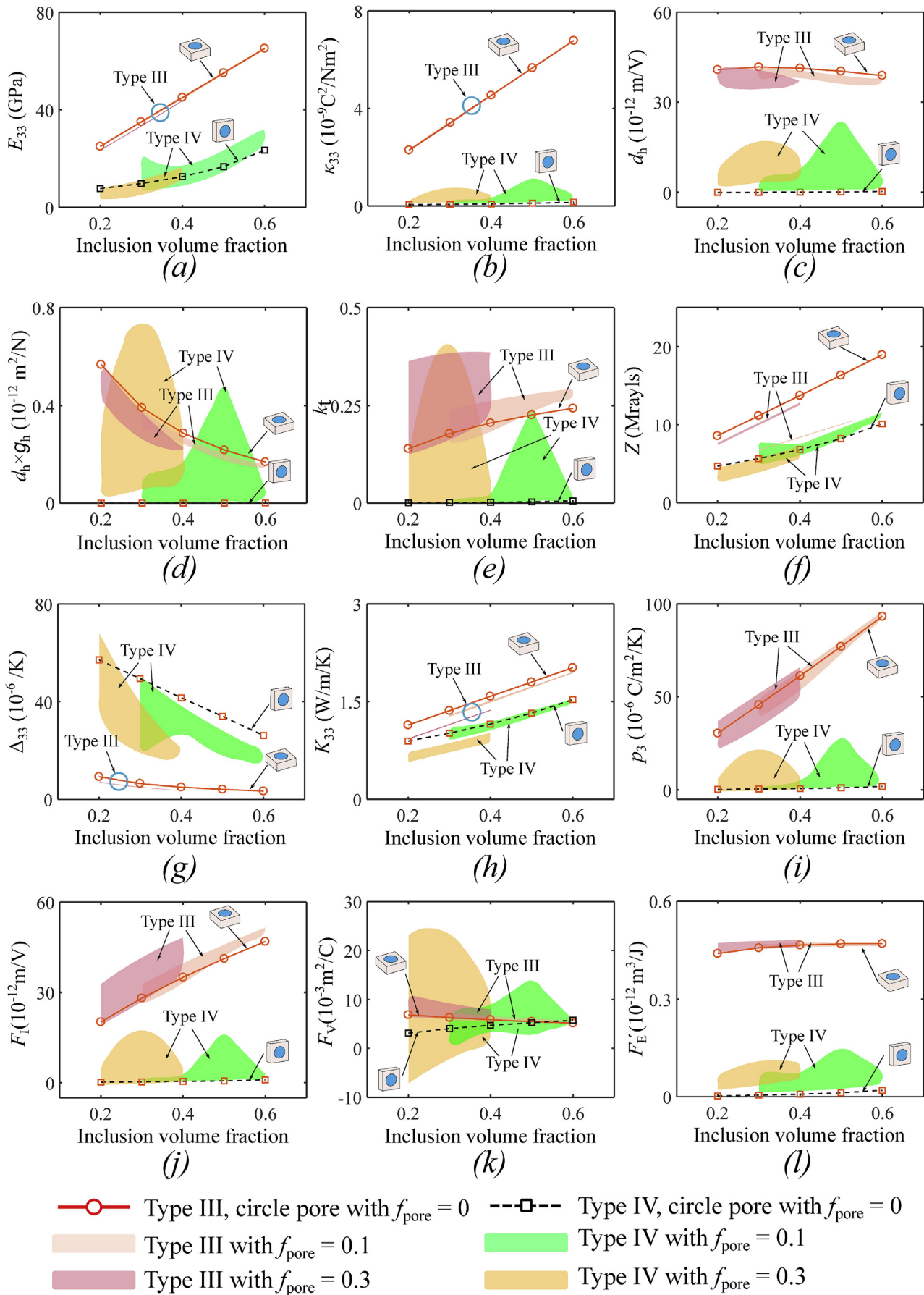


**Fig. 11.** Design charts for thermo-electro-mechanical properties and figures of merit of type III and type IV cellular piezoelectric metamaterials for a wide range of inclusion solid volume fracture  $f_{vi}$  from 0.2 to 0.6.

**Table 4** Comparison of properties of four types of cellular piezoelectric metamaterials with the solid volume fraction of 0.3. The considered type I and type II metamaterials are: regular honeycomb (left),  $c_1 = 0$  and  $c_2 = 0$  (middle) and  $c_1 = -0.4$  and  $c_2 = 0$  (right). From left to right, type III and type IV metamaterials include:  $c_1 = 0$ ,  $c_2 = 0$  and  $f_{\text{pore}} = 0$  (first one),  $c_1 = 0$ ,  $c_2 = 0$  and  $f_{\text{pore}} = 0.1$  (second one),  $c_1 = 0$ ,  $c_2 = 0$  and  $f_{\text{pore}} = 0.3$  (third one),  $c_1 = -0.4$ ,  $c_2 = 0$  and  $f_{\text{pore}} = 0.1$  (fourth one) and  $c_1 = 0$ ,  $c_2 = 0$  and  $f_{\text{pore}} = 0.3$  (fifth one).

	Type I		Type II		Type III		Type IV	
$E_{33}$	1.00	1.00	1.00	0.18	0.46	0.25	1.11	1.09
$k_{33}$	1.00	1.00	1.00	0.63	0.45	0.24	1.01	1.01
$d_{31}$	1.00	1.00	1.00	0.55	0.43	0.23	0.83	0.85
$d_{32}$	1.00	1.00	1.00	0.02	0.02	-0.01	0.83	0.85
$d_{33}$	1.00	1.00	1.00	0.94	0.93	0.90	0.90	0.90
$d_h \times g_h$	1.00	1.01	1.01	3.97	4.17	4.57	1.23	1.19
$k_t$	1.00	1.02	1.02	28.5	39.9	90.4	1.55	1.44
$Z$	1.00	1.02	1.05	0.78	1.00	1.00	0.98	0.98
$\Delta_{33}$	1.00	1.00	0.99	0.98	0.58	0.65	0.47	1.26
$K_{33}$	1.00	1.00	1.00	1.00	1.00	1.00	3.28	2.99
$P_3$	1.00	1.00	1.00	1.01	0.58	0.45	0.24	1.56
$F_1$	1.00	0.95	0.88	0.35	0.44	0.23	1.11	1.19
$F_V$	1.00	0.95	0.88	0.35	0.44	0.23	0.51	0.59
$F_E$	1.00	0.90	0.77	0.21	0.44	0.24	0.26	0.35

pore shapes. Similar numerical works have also been done to optimize the electro-mechanical properties of cellular piezoelectric materials by tailoring the 1–3 microarchitectures [33–37]. It is well-known that, for transverse polarization, electro-mechanical properties of type II metamaterials are sensitive to pore shapes and their figures of merit can be improved [33,34]. The principal elastic, dielectric, and piezoelectric properties decrease monotonically with an increase in the porosity volume fraction. However, increasing porosity in a piezoelectric material, especially for type II metamaterials, enhances the suitability of the smart materials for hydrophone applications [33–37]. This phenomenon has been reported in Section 5.2.1 and 5.2.3. Based on Mori–Tanaka method, it was predicted that type III metamaterials with circular pores showed insensitivity to inclusion and pore volume fraction [30], which is also found in section 5.3.1 and 5.3.3. However, for type III metamaterials, if the circular pore is perpendicular to the polarization direction, increasing inclusion and pore volume fraction will improve the figures of merit [30]. This phenomenon is different with that found for type IV metamaterials, where only  $Z$  (Fig. 11(f)) shows dependence on inclusion volume fraction and all other piezoelectric figures of merit are sensitive to pore shapes. To the best of authors' knowledge, there are only experimental studies on the influence of porous structures on the pyroelectric properties [40,41]. It was reported that increasing porosity decreases pyroelectric coefficient  $p_3$ , but enhances voltage responsivity,  $F_V$ , and pyroelectric harvesting figure of merit,  $F_E$ , of longitudinally and transversely polarized 2-2 porous piezoelectric materials [40]. This result is similar to what we found in Section 5.2.3. However, for longitudinal polarization of 2-2 porous piezoelectric materials, current responsivity  $F_I$  remains the same value while it shows a decreasing trend by increasing porosity for transversely polarized 2-2 porous piezoelectric materials. This is different with type I metamaterials in Fig. 6(g), where  $F_I$  shows a decreasing trend by increasing porosity. The reason for this difference emanates from the adoption of different piezoelectric materials (PZT in Ref. [40] and BaTiO<sub>3</sub> in this paper). An interesting phenomenon provided by type IV metamaterials, whose pyroelectric properties are highly sensitive to pore shapes, are the existence of negative  $p_3$  and  $F_V$ , which is similar as previously reported negative thermal expansion coefficient of bi-material lattices [62].

As expected, different types of metamaterials show dissimilar multifunctional properties. For example, compared to type I, type II metamaterials have smaller elastic modulus in polarization direction,  $E_{33}$ , while possessing larger figures of merit of  $d_h$  and  $d_h \times g_h$ . As shown in Fig. 7, in contrast to obvious difference in  $d_h$  and  $d_h \times g_h$ , since there is not considerable difference between  $Z$ ,  $k_t$ ,  $F_I$ ,  $F_V$  and  $F_E$  of type I and type II metamaterials, the reason for the distinct difference of  $d_h$  and  $d_h \times g_h$  is discussed.

Fig. 13 presents the  $u_3$  displacement and electric displacement  $D_3$  for four types of metamaterials with unit dimensions under three loading conditions A, B and C. All four metamaterials share the same pore shape, where  $c_1 = -0.4$ ,  $c_2 = 0$ ,  $\omega_r = 0$ , and  $s = 1$ . In order to compare the results of these metamaterials, the volume fraction of the BaTiO<sub>3</sub> is the same, where  $f_v = 0.4$  for type I and type II metamaterials and  $f_{vi} = 0.4$  and  $f_{\text{pore}} = 0.1$  for type III and IV metamaterials. ANSYS APDL 18.0 is used for the finite element analysis and a 3D 10-node coupled-field solid element 227 is adopted for discretization. The purpose of loading condition A is to study the elastic compliance or the elastic modulus  $E_{33}$ . Therefore, a unit compression force is applied on the two faces along 3 directions while the other four faces are free and the voltage of the six faces is set as zero to remove the influence of electric field. In addition, the three neutral planes along three directions are constrained to move along their normal directions. It can be seen

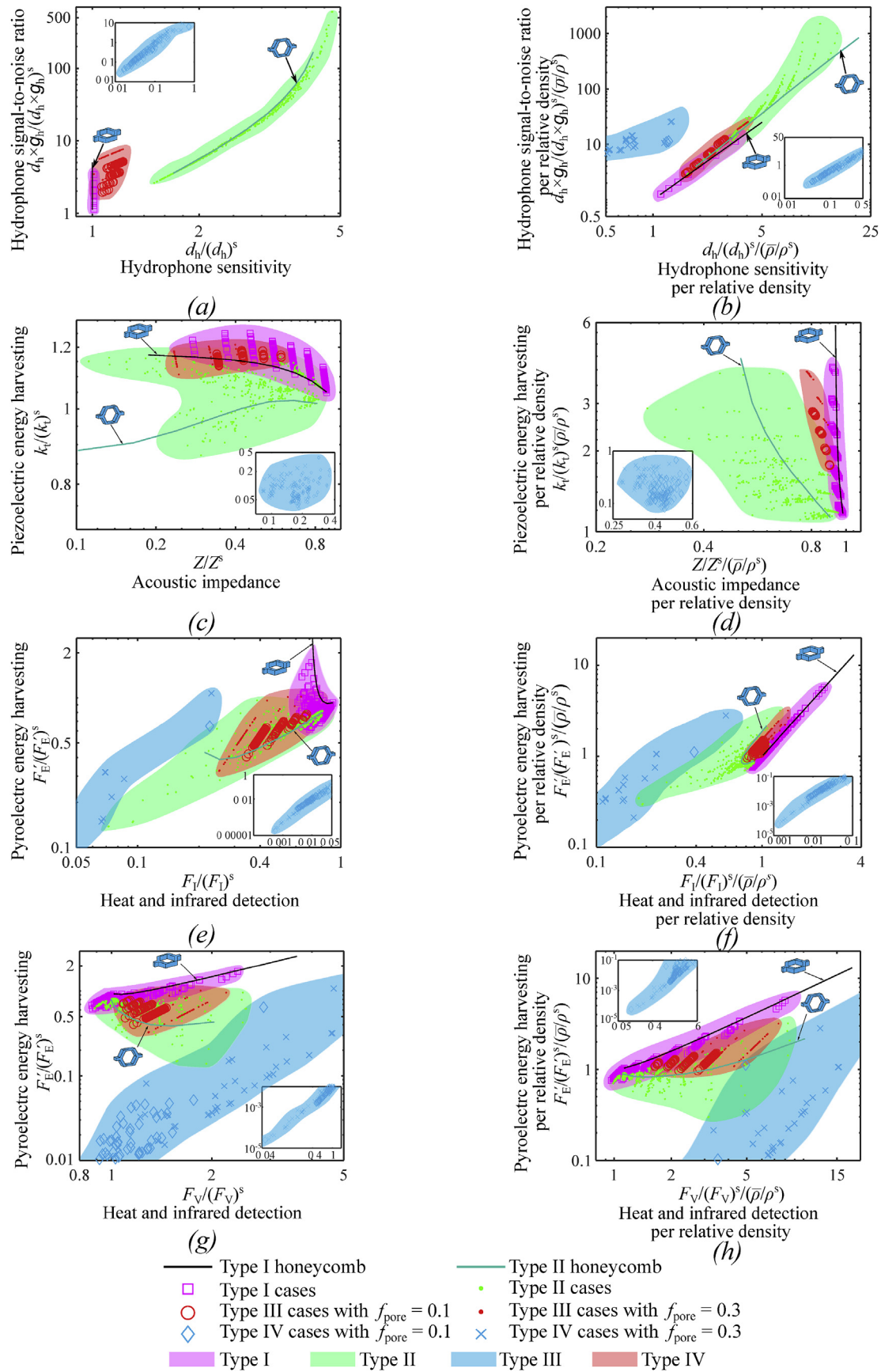


Fig. 12. Comparison between piezoelectric and pyroelectric application of four types of metamaterials.

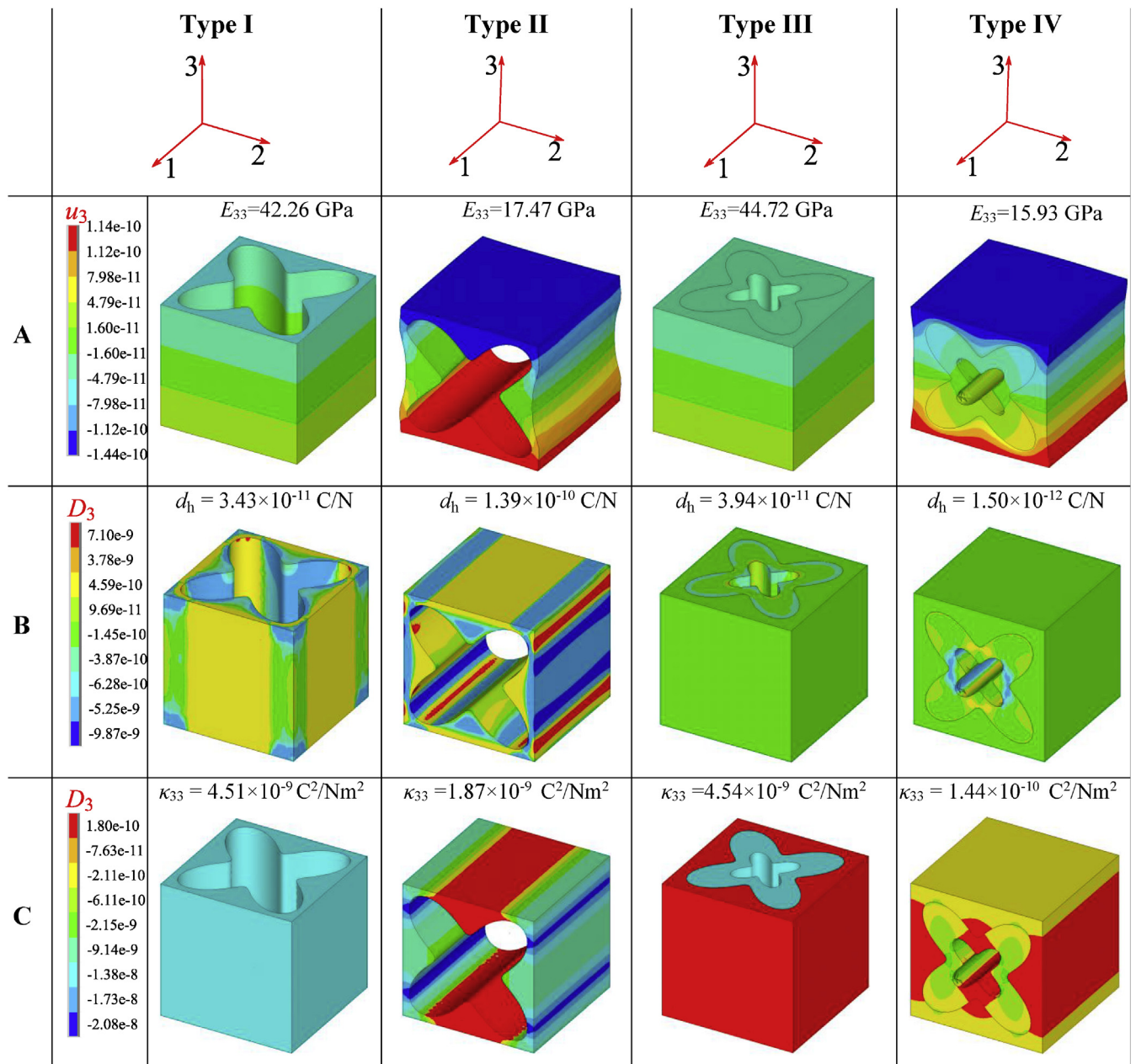


Fig. 13. Response of four types of cellular piezoelectric metamaterials under three loading conditions.

that type I and type III of metamaterials deform by stretching while type II and type IV metamaterials deform by bending. Therefore, type II and type IV metamaterials experience large deformation subjected to compression, indicating their small  $E_{33}$ , while the deformation of type I and type III metamaterials (around  $4.47 \times 10^{-11}$ ) is about one third of the corresponding type II and type IV metamaterials (around  $1.47 \times 10^{-10}$ ).

The physical meaning of  $d_h$  is induced polarization in 3 direction (parallel to the direction that the piezoelectric material is polarized) under unit hydrostatic pressure. In loading condition B, all the six faces are subjected to a unit pressure while the voltage of six faces is set to be zero. Correspondingly, the electric displacement (charge per unit area  $D_3$ ) on the two opposite faces along 3 direction can be used to calculate the induced charge represented as  $d_h$ . Due to its low stiffness, under hydrostatic pressure, type II metamaterials undergo the largest deformation and generates the

highest electric displacement (blue color indicating  $D_3 = -9.87 \times 10^{-19} \text{ C/N}$ ). Therefore, electric charges accumulated on the top and bottom faces are maximized in type II metamaterials; its  $d_h$  is 3.5 times higher than that of type I metamaterials and 93.2 times higher than type IV metamaterials. Type I metamaterials have higher strains compared to type III metamaterials. However,  $d_h$  for type I is only 0.87 times than that of type III metamaterials. This is because adding non-piezoelectric matrix, for type III metamaterials, decreases the coupling of longitudinal and transverse reactions and as a result the absolute value of  $d_{31}$  and  $d_{32}$  becomes smaller, which can be found in Table 4.

As mentioned earlier,  $g_h$  is a hydrostatic voltage coefficient calculated by  $d_h / \kappa_{33}^g$ . Since the variation of  $\kappa_{33}^g$  is due to  $\kappa_{33}$  (Figs. 7 and 11), the piezoelectric permittivity  $\kappa_{33}$  is studied in loading condition C where all six faces are fixed and the voltage of bottom face along 3 direction is 0, while the voltage is 1 V on the top face. In

this condition,  $\kappa_{33}$  is the charges generated on the two faces parallel to the polarization direction. The  $\kappa_{33}$  values for type I and type III metamaterials are close; however,  $\kappa_{33}$  for type III metamaterials is a little higher than type I metamaterials due to the contribution of the matrix. For type II metamaterials, there is no connection between the two opposite faces due to the existence of pore; correspondingly, charges generated on the middle area of the two opposite faces of type II metamaterials are less than that of type I metamaterials. For type IV metamaterials, since the matrix generates minimum electric charges on the two opposite faces, its  $\kappa_{33}$  is as small as 3% of the type I metamaterials.

In general, bending dominant deformation along polarization direction generates more electric charges under hydrostatic pressure leading to a higher  $d_h$ . In addition, introduction of pore along polarization direction decreases  $\kappa_{33}$ . Therefore, type II metamaterials have considerable advantages for  $d_h$ ,  $g_h$  and  $d_h \times g_h$ . For type III metamaterials, the introduction of matrix decreases the absolute value of  $d_{31}$  and  $d_{32}$  and improve  $d_h$  compared to type I metamaterials. Since matrix does not have piezoelectric effects, type IV metamaterials have shown small values for both  $d_h$  and  $\kappa_{33}$ .

## 7. Concluding remarks

Advances in multi-material 3D printing and nanotechnology have opened a new venue for design and manufacturing of smart lightweight materials. In this paper, architected cellular piezoelectric metamaterials with periodic microarchitectures are introduced as a new class of advanced lightweight multifunctional materials with optimized stiffness-to-weight ratio, thermal conductivity, and piezoelectric properties while reducing the consumption of environmentally-incompatible materials (e.g. lead-based piezoelectric materials) in smart structures. The thermo-piezoelectric properties of smart materials with 1–3 type of pores yet to be optimized by tailoring the pore shape and introducing a non-piezoelectric matrix. The current paper conducts a strategic study on the role of pore microarchitecture and non-piezoelectric matrix on effective thermo-electro-mechanical properties of 1–3 type of architected piezoelectric cellular metamaterials. The research leads to the following principal conclusions:

- (1) Asymptotic homogenization can be developed to effectively evaluate the multiphysical performance of cellular piezoelectric metamaterials. We have implemented AH to accurately evaluate elastic, dielectric, piezoelectric, pyroelectric, thermal expansion and thermal conductivity of 1–3 type architected cellular piezoelectric metamaterials for a wide range of pore shapes and solid volume fractions.
- (2)  $E_{33}$ ,  $e_{33}$ ,  $\kappa_{33}$ ,  $K_{33}$ , and four piezoelectric figures of merit of type I cellular piezoelectric metamaterials are insensitive to the pore architecture. However,  $p_3$  and three pyroelectric figures of merit reveal great dependence on the pore architecture. In contrast, apart from thermal expansion and total pyroelectric constants, the other thermo-electro-mechanical properties of type II cellular piezoelectric metamaterials can be improved by optimizing the cell pore shape of smart metamaterials. For example,  $d_h \times g_h$  of an architected cellular piezoelectric metamaterial can be increased by 238% compared to type II honeycomb cellular piezoelectric materials with the same volume fraction, which is appropriate for hydrophone devices.
- (3)  $\Delta_{33}$  and  $\gamma_3$  of architected cellular metamaterials made of single piezoelectric materials are independent of the pore architecture, which has been proved mathematically.
- (4)  $E_{33}$ ,  $\kappa_{33}$ ,  $d_h$ ,  $k_t$ ,  $Z$ ,  $K_{33}$ ,  $p_3$  and  $F_l$  of type III bi-phase metamaterials are always higher than that of type IV bi-phase

metamaterials. In addition, for given pore volume fraction of type III metamaterials, decreasing the inclusion volume fraction is an effective method to improve  $d_h \times g_h$  and  $Z$  for hydrophone device. Furthermore, by tailoring the pore shapes,  $d_h \times g_h$ ,  $F_V$  and  $F'_E$  of type IV metamaterials will exceed those of type III metamaterials. For example, maximum  $d_h \times g_h$ ,  $F_V$  and  $F'_E$  of type IV metamaterials with inclusion volume fraction as 0.3 are 90.3%, 249.1% and 119.3% higher than those of type III piezocomposites with solid circular piezoelectric inclusion.

- (5) Among the four types of cellular piezoelectric metamaterials, type II metamaterials have the best performance on  $d_h$ ,  $d_h \times g_h$  and  $Z$  which reveal their optimum performance for hydrophone devices, while  $E_{33}$ ,  $\kappa_{33}$  and  $K_{33}$  of type III metamaterials are higher than the others. The  $\Delta_{33}$  of type IV metamaterials is always the largest, and  $d_h$ ,  $d_h \times g_h$ ,  $p_3$  and three pyroelectric figures of merit of type IV metamaterials strongly depended on the pore shapes.
- (6) Several factors contribute to the difference among the thermo-electro-mechanical properties of designed cellular piezoelectric metamaterials. For type I metamaterials, stretching deformation mode along the polarization direction results in larger  $E_{33}$ . However, for type II metamaterials, a lower bending dominant stiffness leads to larger deformation and higher hydrostatic charge constants. In some specific conditions, due to the exiting pore between two polarization faces or the existence of a non-piezoelectric matrix, smaller  $\kappa_{33}$  contributes to a higher  $d_h$  and  $d_h \times g_h$  for type II metamaterials and higher  $d_h \times g_h$ ,  $F_V$  and  $F'_E$  for type IV metamaterials.

In conclusion, cellular smart metamaterials with optimized design of microarchitectures can provide exotic mechanical, electromagnetic and optical properties, which have great potential application in the area of optical filter, medical devices, and sensor detection. The presented study sheds light on the possibility of extending property areas of available smart materials by architecting the pore shapes of smart cellular metamaterials to improve their performance for devices working based on the piezoelectric and pyroelectric properties of smart materials. The developed asymptotic homogenization provides an effective method for predicting the multiphysical properties of smart reconfigurable metamaterials with heterogeneous microarchitectures, manufacturable by multi-material additive manufacturing technologies.

## Acknowledgment

A.H. Akbarzadeh acknowledges the financial support by Natural Sciences and Engineering Research Council of Canada through NSERC Discovery Grant RGPIN-2016-0471. J. Shi also acknowledges the financial support provided by the China Scholarship Council [File No. 201706220086] and McGill University.

## Appendix A. Finite element formulation for thermo-piezoelectric field

In this appendix, detailed formulation of the finite element framework for the thermo-piezoelectric field is provided to evaluate the thermo-electro-mechanical properties of cellular piezoelectric metamaterials. In available commercial finite element software, e.g., ANSYS and ABAQUS, the pyroelectric parameter for multiphysics simulation does not exist. As a result, we need to derive the finite element formulation for thermo-electro-mechanical analysis. To provide comprehensive description on uncoupled thermo-piezoelectricity, the empirical Fourier's law for

heat conduction is adopted [63]:

$$q_i = K_{ij} \theta_j \quad (A.1)$$

where  $K_{ij}$  is thermal conductivity tensor,  $\theta_j$  is temperature gradient, and  $q_i$  is the heat flux vector. For linear thermo-piezoelectric materials, based on Eq. (14), the governing differential equations can be written as:

$$\begin{aligned} & \left( C_{ijkl} u_{k,l} \right)_j + \left( e_{ijk} \phi_{,k} \right)_j - \left( \lambda_{ij} \theta \right)_j + b_i = 0 \\ & (e_{kl,i} u_{k,l})_{,i} - (\kappa_{il} \phi_{,l})_{,i} + (p_i \theta)_{,i} - q = 0 \\ & (K_{ij} \theta_j)_{,i} - R = 0 \end{aligned} \quad (A.2)$$

The boundary  $\partial Y$  of domain  $Y$  may include Dirichlet ( $\partial Y_u, \partial Y_\phi, \partial Y_\theta$ ) and/or Neumann ( $\partial Y_\sigma, \partial Y_D, \partial Y_q$ ) parts with  $\partial Y = \partial Y_u \cup \partial Y_\sigma = \partial Y_\phi \cup \partial Y_D = \partial Y_\theta \cup \partial Y_q$  and  $\partial Y_u \cap \partial Y_\sigma = \partial Y_\phi \cap \partial Y_D = \partial Y_\theta \cap \partial Y_q = \emptyset$ , where “ $\cup$ ” and “ $\cap$ ” stand for union and intersection operations, respectively. The boundary conditions can be defined in the following forms:

$$\begin{cases} u_i = \tilde{u}_i & \text{on } \partial Y_u \\ \sigma_{ij} n_j = \tilde{t}_i & \text{on } \partial Y_\sigma \end{cases}, \quad \begin{cases} \phi = \tilde{\phi}_i & \text{on } \partial Y_\phi \\ D_i n_i = -\tilde{D} & \text{on } \partial Y_D \end{cases}, \quad \begin{cases} \theta = \tilde{\theta} & \text{on } \partial Y_\theta \\ q_i n_i = \tilde{q} & \text{on } \partial Y_q \end{cases} \quad (A.3)$$

where wave overbar refers to prescribed values;  $\tilde{u}_i, \tilde{t}_i, \tilde{\phi}_i, \tilde{D}, \tilde{\theta}$ , and  $\tilde{q}$  are the prescribed values of displacement, traction, voltage, free face charge, temperature and heat flux, respectively, while  $\mathbf{n}$  presents the outward normal vector to the boundary of  $\partial Y$ .

An essential step for the finite element modelling of a thermo-piezoelectric medium is to change the governing equations (Eq. (A.2)) into a weak form by Ref. [59]:

$$\begin{aligned} & \int_Y \left( C_{ijkl} u_{k,l} + e_{ijk} \phi_{,k} - \lambda_{ij} \theta \right) w_j dV + \int_Y b_i w_i dV + \int_{\partial Y_\sigma} \tilde{t}_i w_i dS = 0 \\ & \int_Y (e_{kl,i} u_{k,l} - \kappa_{il} \phi_{,l} + p_i \theta) \varphi_{,i} dV - \int_Y q \varphi dV - \int_{\partial Y_D} \tilde{D} \varphi dS = 0 \\ & \int_Y K_{ij} \theta_j \psi_{,i} dV - \int_Y Q \psi dV + \int_{\partial Y_q} \tilde{q} \psi dS = 0 \end{aligned}$$

where  $\mathbf{w}$ ,  $\varphi$  and  $\psi$  are, respectively, admissible functions for displacement, electric potential and temperature which satisfy the boundary conditions introduced in Eq. (A.4).

The next step in finite element modelling, after deriving the weak forms of governing equations, is the discretization of a thermo-piezoelectric medium. For each element, displacement  $\mathbf{u}(\mathbf{x})$ , electric potential  $\varphi(\mathbf{x})$ , and relative temperature  $\theta(\mathbf{x})$  are approximated by a combination of Lagrangian linear shape function  $N_j(\mathbf{x})$  and unknown nodal values  $u_j$ ,  $\varphi_j$  and  $\theta_j$ :

$$\mathbf{u}(\mathbf{x}) = \sum_{j=1}^{N_{nod}} N_j(\mathbf{x}) \mathbf{u}_j, \quad \varphi(\mathbf{x}) = \sum_{j=1}^{N_{nod}} N_j(\mathbf{x}) \varphi_j, \quad \theta(\mathbf{x}) = \sum_{j=1}^{N_{nod}} N_j(\mathbf{x}) \theta_j \quad (A.5)$$

where  $N_{nod}$  is the number of nodes within an element representing the thermo-piezoelectric domain. Analogous to Eq. (A.5), the admissible function can be expressed as:

$$\begin{aligned} \mathbf{w}(\mathbf{x}) &= \sum_{j=1}^{N_{nod}} N_j(\mathbf{x}) \mathbf{w}_j, \quad \varphi(\mathbf{x}) = \sum_{j=1}^{N_{nod}} N_j(\mathbf{x}) \varphi_j, \quad \psi(\mathbf{x}) \\ &= \sum_{j=1}^{N_{nod}} N_j(\mathbf{x}) \psi_j \end{aligned} \quad (A.6)$$

The following strain matrix  $\mathbf{B}_u$ , electric filed matrix  $B_\phi$  and heat flux matrix  $\mathbf{B}_\theta$  provide the relationship between nodal displacement, electric potential and temperature and strain, electric field and heat flux, respectively:

$$\mathbf{B}_u = \mathbf{D}_u^T \mathbf{N}_u, \quad \mathbf{B}_\phi = \mathbf{D}_\phi^T \mathbf{N}_\phi, \quad \mathbf{B}_\theta = \mathbf{D}_\theta^T \mathbf{N}_\theta \quad (A.7)$$

where differential matrices  $\mathbf{D}_u$ ,  $D_\phi$ , and  $\mathbf{D}_\theta$  are defined as:

$$\begin{aligned} w_i &= 0 \quad \text{on } \partial Y_u \\ \varphi &= 0 \quad \text{on } \partial Y_\phi \\ \psi &= 0 \quad \text{on } \partial Y_\theta \end{aligned} \quad (A.4)$$

$$\mathbf{D}_u = \begin{bmatrix} \frac{\partial}{\partial x_1} & 0 & 0 & 0 & \frac{\partial}{\partial x_3} & \frac{\partial}{\partial x_2} \\ 0 & \frac{\partial}{\partial x_2} & 0 & \frac{\partial}{\partial x_3} & 0 & \frac{\partial}{\partial x_1} \\ 0 & 0 & \frac{\partial}{\partial x_3} & \frac{\partial}{\partial x_2} & \frac{\partial}{\partial x_1} & 0 \end{bmatrix}, \quad \mathbf{D}_\phi = \mathbf{D}_\theta = \begin{bmatrix} \frac{\partial}{\partial x_1} \\ \frac{\partial}{\partial x_2} \\ \frac{\partial}{\partial x_3} \end{bmatrix} \quad (A.8)$$

and shape function matrices of  $\mathbf{N}_u$ ,  $\mathbf{N}_\phi$  and  $\mathbf{N}_\theta$  are written as:

$$\mathbf{N}_u = \begin{bmatrix} N_1 & 0 & 0 & N_2 & 0 & 0 & \cdots & N_{Nnod} & 0 & 0 \\ 0 & N_1 & 0 & 0 & N_2 & 0 & \cdots & 0 & N_{Nnod} & 0 \\ 0 & 0 & N_1 & 0 & 0 & N_2 & \cdots & 0 & 0 & N_{Nnod} \end{bmatrix}$$

$$\mathbf{N}_\phi = \mathbf{N}_\theta = [N_1 \ N_2 \ \cdots \ N_{Nnod}] \quad (A.9)$$

In each element volume  $Y_e$ , the weak form of equations can be obtained by substituting Eq. (A.7) into Eq. (A.4):

$$\begin{aligned} \mathbf{w}^T \int_{Y_e} \mathbf{B}_u^T \mathbf{C} \mathbf{B}_u \mathbf{u} + \mathbf{w}^T \int_{Y_e} \mathbf{B}_u^T \mathbf{e} \mathbf{B}_\phi dV \phi - \mathbf{w}^T \int_{Y_e} \mathbf{B}_u^T \lambda \mathbf{B}_\theta dV \theta + \\ \mathbf{w}^T \int_{Y_e} \mathbf{N}_u^T \mathbf{b} dV + \mathbf{w}^T \int_{\partial Y_e} \mathbf{N}_u^T \bar{\mathbf{t}} dS = \mathbf{0} \\ \varphi^T \int_{Y_e} \mathbf{B}_\phi^T \mathbf{e}^T \mathbf{B}_u dV \mathbf{u} - \varphi^T \int_{Y_e} \mathbf{B}_\phi^T \kappa \mathbf{B}_\phi dV \phi + \varphi^T \int_{Y_e} \mathbf{B}_\phi^T \mathbf{p} \mathbf{B}_\theta dV \theta - \\ \varphi^T \int_{Y_e} \mathbf{N}_\phi^T \mathbf{q} dV - \varphi^T \int_{\partial Y_e} \mathbf{N}_\phi^T \bar{\mathbf{q}} dS = \mathbf{0} \\ \psi^T \int_{Y_e} \mathbf{B}_\theta^T \mathbf{K} \mathbf{B}_\theta dV \theta - \psi^T \int_{Y_e} \mathbf{N}_\theta^T \mathbf{r} dV + \psi^T \int_{\partial Y_e} \mathbf{N}_\theta^T \bar{\mathbf{q}} dS = \mathbf{0} \end{aligned} \quad (A.10)$$

From Eq. (A.10), we can extract the element stiffness matrices:

$$\begin{aligned} \mathbf{K}_{uu}^e &= \int_{Y_e} \mathbf{B}_u^T \mathbf{C} \mathbf{B}_u dV, & \mathbf{K}_{u\phi}^e &= \int_{Y_e} \mathbf{B}_u^T \mathbf{e} \mathbf{B}_\phi dV, & \mathbf{K}_{u\theta}^e &= - \int_{Y_e} \mathbf{B}_u^T \lambda \mathbf{B}_\theta dV \\ \mathbf{K}_{\phi u}^e &= \int_{Y_e} \mathbf{B}_\phi^T \mathbf{e}^T \mathbf{B}_u dV, & \mathbf{K}_{\phi\phi}^e &= \int_{Y_e} \mathbf{B}_\phi^T \kappa \mathbf{B}_\phi dV, & \mathbf{K}_{\phi\theta}^e &= \int_{Y_e} \mathbf{B}_\phi^T \mathbf{p} \mathbf{B}_\theta dV \\ \mathbf{K}_{\theta\theta}^e &= \int_{Y_e} \mathbf{B}_\theta^T \mathbf{K} \mathbf{B}_\theta dV \end{aligned} \quad (A.11)$$

and element force vectors:

$$\begin{aligned} \mathbf{f}_u^e &= \int_{Y_e} \mathbf{N}_u^T \mathbf{b} dV + \int_{\partial Y_e} \mathbf{N}_u^T \bar{\mathbf{t}} dS \\ \mathbf{f}_\phi^e &= - \int_{Y_e} \mathbf{N}_\phi^T \mathbf{q} dV - \int_{\partial Y_e} \mathbf{N}_\phi^T \bar{\mathbf{q}} dS \\ \mathbf{f}_\theta^e &= - \int_{Y_e} \mathbf{N}_\theta^T \mathbf{r} dV + \int_{\partial Y_e} \mathbf{N}_\theta^T \bar{\mathbf{q}} dS \end{aligned} \quad (A.12)$$

After assembling the stiffness matrices and force vectors for all elements, we can obtain the governing equations for cellular piezoelectric metamaterials:

$$\begin{bmatrix} \mathbf{K}_{uu} & \mathbf{K}_{u\phi} & \mathbf{K}_{u\theta} \\ \mathbf{K}_{\phi u} & \mathbf{K}_{\phi\phi} & \mathbf{K}_{\phi\theta} \\ \mathbf{0} & \mathbf{0} & \mathbf{K}_{\theta\theta} \end{bmatrix} \begin{pmatrix} \mathbf{u} \\ \phi \\ \theta \end{pmatrix} = \begin{pmatrix} \mathbf{f}_u \\ \mathbf{f}_\phi \\ \mathbf{f}_\theta \end{pmatrix} \quad (A.13)$$

where all local stiffness matrices and force subvectors have been assembled. In this paper, MATLAB software is used to write the finite element code for thermo-electro-mechanical analysis of cellular piezoelectric metamaterials, while the quadratic tetrahedron element, which is more accurate than a linear element and is suitable for meshing irregular structures designed in this paper, is adopted for discretizing the thermo-piezoelectric medium.

## Appendix B. Initial loading and periodic boundary conditions for local problem

In order to obtain the effective thermo-electro-mechanical properties from Eq. (29), three kinds of differential equations, namely Eqs. (25) – (27), should be solved. Based on the finite element method (Appendix A), the force vectors (Eq. (A.12)) for these three local problems have physical meaning. In fact, they are specific cases of initial strain loads, electric field intensity loadings or thermal loadings. Due to the variation of  $m$  and  $n$  in Eq. (24), six specific initial mechanical loads should be considered for Eq. (25):

$$\begin{aligned} \boldsymbol{\epsilon}^{11} &= [1, 0, 0, 0, 0, 0], \mathbf{E}^{11} = [0, 0, 0], \theta^{11} = 0 \\ \boldsymbol{\epsilon}^{22} &= [0, 1, 0, 0, 0, 0], \mathbf{E}^{22} = [0, 0, 0], \theta^{22} = 0 \\ \boldsymbol{\epsilon}^{33} &= [0, 0, 1, 0, 0, 0], \mathbf{E}^{33} = [0, 0, 0], \theta^{33} = 0 \\ \boldsymbol{\epsilon}^{23} &= [0, 0, 0, 1, 0, 0], \mathbf{E}^{23} = [0, 0, 0], \theta^{23} = 0 \\ \boldsymbol{\epsilon}^{13} &= [0, 0, 0, 0, 1, 0], \mathbf{E}^{13} = [0, 0, 0], \theta^{13} = 0 \\ \boldsymbol{\epsilon}^{12} &= [0, 0, 0, 0, 0, 1], \mathbf{E}^{12} = [0, 0, 0], \theta^{12} = 0 \end{aligned} \quad (B.1)$$

Similarly, three specific initial electrical loads should be used in Eq. (26):

$$\begin{aligned}\boldsymbol{\varepsilon}^1 &= [0, 0, 0, 0, 0, 0], \boldsymbol{E}^1 = [1, 0, 0], \theta^1 = 0 \\ \boldsymbol{\varepsilon}^2 &= [0, 0, 0, 0, 0, 0], \boldsymbol{E}^2 = [0, 1, 0], \theta^2 = 0 \\ \boldsymbol{\varepsilon}^3 &= [0, 0, 0, 0, 0, 0], \boldsymbol{E}^3 = [0, 0, 1], \theta^3 = 0\end{aligned}\quad (\text{B.2})$$

and one initial thermal load is needed for Eq. (27):

$$\boldsymbol{\varepsilon} = [0, 0, 0, 0, 0, 0], \boldsymbol{E} = [0, 0, 0], \theta = 1 \quad (\text{B.3})$$

Based on Eqs. (B.1) – (B.3), the elements of force vector introduced in Eq. (A.12) are expressed for different  $m$  and  $n$  as follows:

$$\mathbf{f}_u^e = \int_{Y_e} \mathbf{N}_u^T \mathbf{C} \boldsymbol{\varepsilon}^{mn} dV, \quad \mathbf{f}_\phi^e = - \int_{Y_e} \mathbf{N}_\phi^T \boldsymbol{E}^{mn} dV, \quad \mathbf{f}_\theta^e = - \int_{Y_e} \mathbf{N}_\theta^T \boldsymbol{q}^{mn} dV \quad (\text{B.4})$$

To evaluate the effective thermo-electro-mechanical properties of cellular piezoelectric metamaterials, we also need to apply

$$\begin{aligned}& \left\langle C_{ijmn}^* + C_{ijkl}^* M U_{k,l}^{mn} + e_{ijl}^* N U_{l,m}^{mn} \right\rangle \overline{\Delta_{mn}} + \left\langle e_{ijn}^* + C_{ijkl}^* M \Phi_{k,l}^n + e_{ijl}^* N \Phi_{l,m}^n \right\rangle \overline{\gamma_n} = \\ & \left\langle C_{ijmn}^* \Delta_{mn}^* + e_{ijn}^* \gamma_n^* - C_{ijkl}^* M \Theta_{k,l} - e_{ijl}^* N \Theta_{l,m} \right\rangle \\ & \left\langle e_{mni}^* + e_{ikl}^* M U_{k,l}^{mn} - \kappa_{il}^* N U_{l,m}^{mn} \right\rangle \overline{\Delta_{mn}} - \left\langle \kappa_{in}^* - e_{ikl}^* M \Phi_{k,l}^n + \kappa_{il}^* N \Phi_{l,m}^n \right\rangle \overline{\gamma_n} = \\ & \left\langle e_{mni}^* \Delta_{mn}^* - \kappa_{in}^* \gamma_n^* - e_{ikl}^* M \Theta_{k,l} + \kappa_{il}^* N \Theta_{l,m} \right\rangle\end{aligned}\quad (\text{C.3})$$

periodic boundary conditions to RVE and then solve these finite element equations on this porous thermo-piezoelectric medium. Due to the periodicity of the microscopic scale, displacement, electric potential and temperature of local problems are symmetric on opposite faces of RVE. For three pairs of opposite RVE faces (Fig. 4(b)), we have:

$$\begin{aligned}\mathbf{u}^{y_{1+}} - \mathbf{u}^{y_{1-}} &= 0, \boldsymbol{\phi}^{y_{1+}} - \boldsymbol{\phi}^{y_{1-}} = 0, \theta^{y_{1+}} - \theta^{y_{1-}} = 0 \\ \mathbf{u}^{y_{2+}} - \mathbf{u}^{y_{2-}} &= 0, \boldsymbol{\phi}^{y_{2+}} - \boldsymbol{\phi}^{y_{2-}} = 0, \theta^{y_{2+}} - \theta^{y_{2-}} = 0 \\ \mathbf{u}^{y_{3+}} - \mathbf{u}^{y_{3-}} &= 0, \boldsymbol{\phi}^{y_{3+}} - \boldsymbol{\phi}^{y_{3-}} = 0, \theta^{y_{3+}} - \theta^{y_{3-}} = 0\end{aligned}\quad (\text{B.5})$$

where  $u^{y_i}$ ,  $\phi^{y_i}$  and  $\theta^{y_i}$  represent, respectively, displacement, electric potential and temperature on the  $i$ th face of RVE.

### Appendix C. Constant thermal expansion and total pyroelectric coefficients of cellular metamaterials made of single piezoelectric material

To support the numerical observation presented in Section 5.2, we mathematically prove that the vector  $\overline{\Delta}$ , representing the

effective thermal expansion and total pyroelectric coefficients, is independent of the microarchitecture (volume fraction and cell topology) of the cellular piezoelectric metamaterials made of a single piezoelectric materials (see Fig. 6(e)). Based on Eqs. (11) – (13), the thermal stress tensor  $\lambda_{ij}$  and pyroelectric tensor  $p_i$  can be expressed as:

$$\begin{aligned}C_{ijkl} \Delta_{kl} + e_{ijk} \gamma_k &= \lambda_{ij} \\ e_{kli} \Delta_{kl} - \kappa_{ik} \gamma_k &= p_i\end{aligned}\quad (\text{C.1})$$

Combining Eq. (29) and Eq. (C.1), the effective thermal stress tensor  $\lambda_{ij}$  and pyroelectric tensor  $p_i$  can be rewritten as:

$$\begin{aligned}\overline{C_{ijmn} \Delta_{mn}} + \overline{e_{ijn} \gamma_n} &= \overline{\lambda_{ij}} \\ \overline{e_{mni} \Delta_{mn}} - \overline{\kappa_{in} \gamma_n} &= \overline{p_i}\end{aligned}\quad (\text{C.2})$$

or:

where  $\overline{\Delta_{kl}}$  and  $\overline{\gamma_k}$  refer to the effective thermal expansion and total pyroelectric coefficients. In order to determine these coefficients, the relationship between the solutions of local problems (Eqs. (25) – (27)) should be first identified.

Substituting Eq. (C.1) into Eq. (27), the third local problem can be rewritten as:

$$\begin{aligned}C_{ijkl}^* M \Theta_{k,l} + e_{kij}^* N \Theta_{k,l} &= C_{ijkl} \Delta_{kl} + e_{ijk} \gamma_k \\ e_{kli}^* M \Theta_{k,l} - \kappa_{il}^* N \Theta_{k,l} &= e_{ikl} \Delta_{kl} - \kappa_{ik} \gamma_k\end{aligned}\quad (\text{C.4})$$

Comparing Eq. (C.4), Eqs. (25) and (26), it can be found that the solutions of the three local problems satisfy the following relationship:

$$\begin{aligned}M \Theta_{k,l} &= -\Delta_{mn} M U_{k,l}^{mn} - \gamma_n M \Phi_{k,l}^n \\ N \Theta_{k,l} &= -\Delta_{mn} N U_{l,m}^{mn} - \gamma_n N \Phi_{l,m}^n\end{aligned}\quad (\text{C.5})$$

Substituting Eq. (C.5) into the right side of Eq. (C.3), the following expression can be obtained:

$$\begin{aligned}& \left\langle C_{ijmn}^* \Delta_{mn} + e_{ijn}^* \gamma_n^* - C_{ijkl}^* M \Theta_{k,l} - e_{ijl}^* N \Theta_{l,m} \right\rangle \\ & = \left\langle C_{ijmn}^* \Delta_{mn} + e_{ijn}^* \gamma_n^* + C_{ijkl}^* \left( M U_{k,l}^{mn} \Delta_{mn} + M \Phi_{k,l}^n \gamma_n^* \right) + e_{ijl}^* \left( N U_{l,m}^{mn} \Delta_{mn} + N \Phi_{l,m}^n \gamma_n^* \right) \right\rangle \\ & = \left\langle C_{ijmn}^* \Delta_{mn} + C_{ijkl}^* M U_{k,l}^{mn} \Delta_{mn} + e_{ijl}^* N U_{l,m}^{mn} \Delta_{mn} \right\rangle + \left\langle e_{ijn}^* \gamma_n^* + C_{ijkl}^* M \Phi_{k,l}^n \gamma_n^* + e_{ijl}^* N \Phi_{l,m}^n \gamma_n^* \right\rangle\end{aligned}\quad (\text{C.6})$$

and:

$$\begin{aligned}
 & \left\langle e_{mni}^* \Delta_{mn}^* - \kappa_{in}^* \gamma_n^* - e_{ikl}^* M \Theta_{+k,l} \kappa_{il}^* N \Theta_{,l} \right\rangle \\
 &= \left\langle e_{mni}^* \Delta_{mn}^* - \kappa_{in}^* \gamma_n^* + e_{ikl}^* (M U_{k,l}^{mn} \Delta_{mn} + M \Phi_{k,l}^n \gamma_n) - \kappa_{il}^* (N U_{,l}^{mn} \Delta_{mn} + N \Phi_{,l}^n \gamma_n) \right\rangle \\
 &= \left\langle e_{mni}^* \Delta_{mn}^* + e_{ikl}^* M U_{k,l}^{mn} \Delta_{mn} - \kappa_{il}^* N U_{,l}^{mn} \Delta_{mn} \right\rangle - \left\langle \kappa_{in}^* \gamma_n^* - e_{ikl}^* M \Phi_{k,l}^n \gamma_n + \kappa_{il}^* N \Phi_{,l}^n \gamma_n \right\rangle
 \end{aligned} \tag{C.7}$$

For cellular piezoelectric metamaterials made of a single piezoelectric material, the thermo-electro-mechanical properties within the pore are zero while they are constant and non-zero within the solid part of the cellular metamaterials. Therefore, Eqs. (C.6) and (C.7) can be rewritten as:

$$\begin{aligned}
 & \left\langle C_{ijmn}^* \Delta_{mn}^* + e_{ijn}^* \gamma_n^* - C_{ijkl}^* M \Theta_{k,l} - e_{ijl}^* N \Theta_{,l} \right\rangle \\
 &= \left\langle C_{ijmn}^s + C_{ijkl}^s M U_{k,l}^{mn} + e_{ijl}^s N U_{,l}^{mn} \right\rangle \Delta_{mn}^s + \left\langle e_{ijn}^s \chi + C_{ijkl}^s M \Phi_{k,l}^n \gamma_n^s + e_{ijl}^s N \Phi_{,l}^n \gamma_n^s \right\rangle \gamma_n^s
 \end{aligned} \tag{C.8}$$

and:

$$\begin{aligned}
 & \left\langle e_{mni}^* \Delta_{mn}^* - \kappa_{in}^* \gamma_n^* - e_{ikl}^* M \Theta_{+k,l} \kappa_{il}^* N \Theta_{,l} \right\rangle \\
 &= \left\langle e_{mni}^s + e_{ikl}^s M U_{k,l}^{mn} \Delta_{mn} - \kappa_{il}^s N U_{,l}^{mn} \right\rangle \Delta_{mn}^s - \left\langle \kappa_{in}^s - e_{ikl}^s M \Phi_{k,l}^n + \kappa_{il}^s N \Phi_{,l}^n \right\rangle \gamma_n^s
 \end{aligned} \tag{C.9}$$

where the superscript "s" stands for the properties of solid material.

Comparing Eqs. (C.8) and (C.9) with the left side of Eq. (C.3) and considering that  $C^* = C^s$ ,  $e^* = e^s$ , and  $\kappa^* = \kappa^s$ , we can conclude that:

$$\overline{\Delta_{mn}} = \Delta_{mn}^s, \quad \overline{\gamma_n} = \gamma_n^s \tag{C.10}$$

which means that the effective thermal expansion  $\overline{\Delta_{mn}}$  and total pyroelectric coefficients  $\overline{\gamma_n}$  for cellular metamaterials made of single piezoelectric material are the same as its corresponding properties of parent solid piezoelectric materials independent of its cell microarchitecture.

## Appendix D. Supplementary data

Supplementary data to this article can be found online at <https://doi.org/10.1016/j.actamat.2018.10.001>.

## References

- [1] V.G. Veselago, The electrodynamics of substances with simultaneously negative values of  $\epsilon$  and  $\mu$ , Sov. Phys. Usp. 10 (4) (1968) 509.
- [2] A.N. Lagarkov, V.N. Semenenko, V.A. Chistyakov, D.E. Ryabov, S.A. Tretyakov, C.R. Simovski, Resonance properties of bi-helix media at microwaves, Electromagnetics 17 (3) (1997) 213–237.
- [3] D.R. Smith, J.B. Pendry, M.C.K. Wiltshire, Metamaterials and negative refractive index, Science 305 (5685) (2004) 788–792.
- [4] V.M. Shalaev, W. Cai, U.K. Chettiar, K. Yuan, A. Sarychev, V. Drachev, A. Kildishev, Negative index of refraction in optical metamaterials, Optic Lett. 30 (24) (2005) 3356–3358.
- [5] V.M. Shalaev, Optical negative-index metamaterials, Nat. Photon. 1 (1) (2007) 41–48.
- [6] J. Li, C.T. Chan, Double-negative acoustic metamaterial, Phys. Rev. 70 (2) (2004), 055602.
- [7] H. Chen, C.T. Chan, Acoustic cloaking in three dimensions using acoustic metamaterials, Appl. Phys. Lett. 91 (18) (2007), 183518.
- [8] A. Rafsanjani, A.H. Akbarzadeh, D. Pasini, Snapping mechanical metamaterials under tension, Adv. Mater. 27 (39) (2015) 5931–5935.
- [9] J.T.B. Overvelde, K. Bertoldi, Relating pore shape to the non-linear response of periodic elastomeric structures, J. Mech. Phys. Solid. 64 (1) (2014) 351–366.
- [10] S. Babaei, J. Shim, J.C. Weaver, E. Chen, N. Patel, K. Bertoldi, 3D soft metamaterials with negative Poisson's ratio, Adv. Mater. 25 (36) (2013)

- 5044–5049.
- [11] J.T.B. Overvelde, T.A.D. Jong, Y. Shevchenko, S.A. Becerra, J. Whitesides, J. Weaver, C. Hoberman, K. Bertoldi, A three-dimensional actuated origami-inspired transformable metamaterial with multiple degrees of freedom, *Nat. Commun.* 7 (2016), 10929.
- [12] M.G. Lee, J.W. Lee, S.C. Han, K. Kang, Mechanical analyses of "Shellular", an ultralow-density material, *Acta Mater.* 103 (8) (2016) 595–607.
- [13] M. Maldovan, Sound and heat revolutions in phononics, *Nature* 503 (7475) (2013) 209–217.
- [14] S. Narayana, Y. Sato, Heat flux manipulation with engineered thermal materials, *Phys. Rev. Lett.* 108 (21) (2012), 214303.
- [15] T. Shimada, V.L. Le, K. Nagano, J. Wang, T. Kitamura, Hierarchical ferroelectric and ferrotoroidal polarizations coexistent in nano-metamaterials, *Science Report* 5 (2015), 14653.
- [16] V.L. Le, T. Shimada, S. Sepideh, J. Wang, T. Kitamura, Polar and toroidal electromechanical properties designed by ferroelectric nano-metamaterials, *Acta Mater.* 113 (2016) 81–89.
- [17] S. Bodkhe, G. Turcot, F.P. Gosselin, D. Therriault, One-step solvent evaporation-assisted 3D printing of piezoelectric PVDF nanocomposite structures, *ACS Appl. Mater. Interfaces* 9 (24) (2017), 20833.
- [18] J. Briscoe, S. Dunn, Piezoelectric nanogenerators – a review of nanostructured piezoelectric energy harvesters, *Nanomater. Energy* 14 (2015) 15–29.
- [19] R. Kargupta, C. Marcheselli, T.A. Venkatesh, Electromechanical response of 1–3 piezoelectric composites: effect of fiber shape, *J. Appl. Phys.* 104 (2) (2008), 024105.
- [20] R. Kar-Gupta, T.A. Venkatesh, Electromechanical response of piezoelectric composites: effects of geometric connectivity and grain size, *Acta Mater.* 56 (15) (2008) 3810–3823.
- [21] C. Marcheselli, T.A. Venkatesh, Electromechanical response of 1–3 piezoelectric composites with hollow fibers, *Appl. Phys. Lett.* 93 (2) (2008), 322903.
- [22] S. Iyer, T.A. Venkatesh, Electromechanical response of (3–0, 3–1) particulate, fibrous, and porous piezoelectric composites with anisotropic constituents: a model based on the homogenization method, *Int. J. Solid Struct.* 51 (6) (2014) 1221–1234.
- [23] R.D. Medeiros, R. Rodríguez-Ramos, R. Guinovart-Díaz, J. Bravo-Castillero, J. Otero, V. Tita, Numerical and analytical analyses for active fiber composite piezoelectric composite materials, *J. Intell. Mater. Syst. Struct.* 26 (1) (2015) 101–118.
- [24] M.L. Feng, C.C. Wu, A study of three-dimensional four-step braided piezoceramic composites by the homogenization method, *Compos. Sci. Technol.* 61 (13) (2001) 1889–1898.
- [25] S. Kari, H. Berger, R. Rodriguez-Ramos, U. Gabbert, Numerical Evaluation of effective material properties of transversely randomly distributed unidirectional piezoelectric fiber composites, *J. Intell. Mater. Syst. Struct.* 18 (4) (2007) 361–372.
- [26] R. Guinovart-Díaz, P. Yan, R. Rodríguez-Ramos, J.C. López-Realpozo, C.P. Jiang, J. Bravo-Castillero, F.J. Sabina, Effective properties of piezoelectric composites with parallelogram periodic cells, *Int. J. Eng. Sci.* 53 (4) (2012) 58–66.
- [27] S.L. Vatanabe, G.H. Paulino, E.C.N. Silva, Design of functionally graded piezocomposites using topology optimization and homogenization – toward effective energy harvesting materials, *Comput. Methods Appl. Mech. Eng.* 266 (11) (2013) 205–218.
- [28] A. Deraemaeker, H. Nasser, Numerical evaluation of the equivalent properties of Macro Fiber Composite (MFC) transducers using periodic homogenization, *Int. J. Solid Struct.* 47 (24) (2010) 3272–3285.
- [29] R. Haj-Ali, H. Zemer, R. El-Hajjar, J. Aboudi, Piezoresistive fiber-reinforced composites: a coupled nonlinear micromechanical–microelectrical modeling approach, *Int. J. Solid Struct.* 51 (2) (2014) 491–503.
- [30] C.N. Delta, D. Shu, The performance of 1–3 piezoelectric composites with a porous non-piezoelectric matrix, *Acta Mater.* 56 (4) (2008) 754–761.
- [31] J. Bravo-Castillero, R. Rodríguez-Ramos, R. Guinovart-Díaz, J. Sabina F, R. Aguiar A, P. Silva U, J. LuisGómez-Muñoz, Analytical formulae for electromechanical effective properties of 3–1 longitudinally porous piezoelectric materials, *Acta Mater.* 57 (3) (2009) 795–803.
- [32] S. Iyer, T.A. Venkatesh, Electromechanical response of (0–3) porous piezoelectric materials: effects of porosity shape, *J. Appl. Phys.* 110 (3) (2011), 034109.
- [33] R. Kar-Gupta, T.A. Venkatesh, Electromechanical response of porous piezoelectric materials: effects of porosity distribution, *Appl. Phys. Lett.* 93 (1) (2007), 062904–1.
- [34] R. Kar-Gupta, T.A. Venkatesh, Electromechanical response of porous piezoelectric materials, *Appl. Phys. Lett.* 54 (15) (2006) 4063–4078.
- [35] S. Iyer, M. Alkhader, T.A. Venkatesh, Electromechanical behavior of auxetic piezoelectric cellular solids, *Scripta Mater.* 99 (2015) 65–68.
- [36] S. Iyer, M. Alkhader, T.A. Venkatesh, Electromechanical response of piezoelectric honeycomb foam structures, *J. Am. Ceram. Soc.* 97 (3) (2014) 826–834.
- [37] S. Iyer, M. Alkhader, T.A. Venkatesh, On the relationships between cellular structure, deformation modes and electromechanical properties of piezoelectric cellular solids, *Int. J. Solid Struct.* 80 (2016) 73–83.
- [38] K.S. Challagulla, T.A. Venkatesh, Electromechanical response of piezoelectric foams, *Acta Mater.* 60 (5) (2012) 2111–2127.
- [39] P.W. Bosse, K.S. Challagulla, T.A. Venkatesh, Effects of foam shape and porosity aspect ratio on the electromechanical properties of 3–3 piezoelectric foams, *Acta Mater.* 60 (19) (2012) 6464–6475.
- [40] Y. Zhang, M. Xie, J. Roscow, Y.X. Bao, K.C. Zhou, D. Dou Zhang, C.R. Bowen, Enhanced pyroelectric and piezoelectric properties of PZT with aligned porosity for energy harvesting applications, *J. Mater. Chem. A Mater. Energy Sustain.* 5 (14) (2017) 6569.
- [41] A. Navid, C.S. Lynch, L. Pilon, Purified and porous poly (vinylidene fluoride-trifluoroethylene) thin films for pyroelectric infrared sensing and energy harvesting, *Smart Mater. Struct.* 19 (5) (2010), 055006.
- [42] J.D. Eshelby, The determination of the elastic field of an ellipsoidal inclusion, and related problems, *Proc. Roy. Soc. Lond.* 241 (1226) (1957) 376–396.
- [43] B. Wang, Three-dimensional analysis of an ellipsoidal inclusion in a piezoelectric material, *Int. J. Solid Struct.* 29 (1992) 293–308.
- [44] M.L. Dunn, M. Taya, Micromechanics predictions of the effective electroelastic moduli of piezoelectric composites, *Int. J. Solid Struct.* 30 (2) (1993) 161–175.
- [45] T. Chen, Piezoelectric properties of multiphase fibrous composites: some theoretical results, *J. Mech. Phys. Solid.* 41 (11) (1993) 1781–1794.
- [46] E.M. Hassan, A.L. Kalamkarov, A.V. Georgiades, K. Challagulla, An asymptotic homogenization model for smart 3D grid-reinforced composite structures with generally orthotropic constituents, *Smart Mater. Struct.* 18 (7) (2012) 5844–5877.
- [47] A.L. Kalamkarov, I.V. Andrianov, V.V. Danishevskyy, Asymptotic homogenization of composite materials and structures, *Appl. Mech. Rev.* 62 (3) (2009) 669–676.
- [48] H. Berger, S. Kari, U. Gabbert, R. Reinaldo, R. Guinovart, J. Otero, B. Julian, An analytical and numerical approach for calculating effective material coefficients of piezoelectric fiber composites, *Int. J. Solid Struct.* 42 (21) (2005) 5692–5714.
- [49] J.T.B. Overvelde, S. Shan, K. Bertoldi, Compaction through buckling in 2D periodic, soft and porous structures: effect of pore shape, *Adv. Mater.* 24 (17) (2012) 2337–2342.
- [50] M.C. Dökmeci, Vibrations of piezoelectric crystals, *Int. J. Eng. Sci.* 18 (3) (1980) 431–448.
- [51] M. Cho, J. Oh, Higher order zig-zag theory for fully coupled thermo-electric–mechanical smart composite plates, *Int. J. Solid Struct.* 41 (5–6) (2004) 1331–1356.
- [52] H. Parkus, *Thermoelasticity*, second ed., Springer, New York, 1976.
- [53] A.H. Akbarzadeh, M.H. Babaei, Z.T. Chen, Coupled thermopiezoelectric behavior of a one-dimensional FGP medium based on C-T theory, *P I MECH ENG C-J MEC* 225 (01) (2011) 2537–2551.
- [54] M.L. Dunn, Micromechanics of coupled electroelastic composites: effective thermal expansion and pyroelectric coefficients, *J. Appl. Phys.* 73 (10) (1993) 5131–5140.
- [55] A.H. Akbarzadeh, D. Pasini, Multiphysics of multilayered and functionally graded cylinders under prescribed hydrothermomegnetoelastomechanical loading, *J. Appl. Mech.* 81 (4) (2014), 041018.
- [56] A.H. Akbarzadeh, M.H. Babaei, Z.T. Chen, Thermopiezoelectric analysis of a functionally graded piezoelectric, *Int. J. Appl. Mech.* 03 (01) (2011), 1100086.
- [57] Y. Zhang, M. Xie, J. Roscow, Y. Bao, K. Zhou, D. Zhang, C. Bowen, Enhanced pyroelectric and piezoelectric properties of PZT with aligned porosity for energy harvesting applications, *J. Mater. Chem.: Mater. Energy & Sustain.* 5 (14) (2017) 6569–6580.
- [58] S. Arabnejad, D. Pasini, Mechanical properties of lattice materials via asymptotic homogenization and comparison with alternative homogenization methods, *Int. J. Mech. Sci.* 77 (4) (2013) 249–262.
- [59] F. Fantoni, A. Bacigalupo, M. Paggi, Multi-field asymptotic homogenization of thermo-piezoelectric materials with periodic microstructure, *Int. J. Solid Struct.* 120 (2017) 31–56.
- [60] K. Yao, F. Biscani, S. Belouettar, H. Nasser, E. Carrera, Multi-coating inhomogeneities approach for the effective thermo-electro-elastic properties of piezoelectric composite materials, *Compos. Struct.* 92 (4) (2010) 964–972.
- [61] H. Yi, Heat capacity, thermal conductivity, and thermal expansion of barium titanate-based ceramics, *Thermochim. Acta* 419 (1) (2004) 135–141.
- [62] R. Lakes, Cellular solid structures with unbounded thermal expansion, *J. Mater. Sci. Lett.* 15 (6) (1996) 475–477.
- [63] A.H. Akbarzadeh, Y. Cui, Z.T. Chen, Thermal wave: from nonlocal continuum to molecular dynamics, *RSC Adv.* 7 (22) (2017) 13623–13636.